Evidence for the development of permeability anisotropy in lava domes and volcanic conduits.

Jamie I. Farquharson[1], Michael J. Heap[1], Yan Lavallée[2], Nick R. Varley[3], Patrick Baud[1]

[1]*Équipe de Géophysique Expérimentale, Institut de Physique de Globe de Strasbourg (UMR 7516 CNRS, Université de Strasbourg/EOST), 5 rue René Descartes, 67084 Strasbourg cedex, France.*

[2]*Earth, Ocean and Ecological Sciences, University of Liverpool, Liverpool L69 3GP, United Kingdom.*

[3]*Facultad de Ciencias, University of Colima, Colima 28045, Mexico.*

Corresponding author: J. Farquharson (farquharson@unistra.fr)

Abstract

The ease at which exsolving volatiles can migrate though magma and outgas influences the explosivity of a volcanic eruption. Volcanic rocks often contain discrete discontinuities, providing snapshots of strain localisation processes that occur during magma ascent and extrusion. Whether these features comprise pathways for or barriers to fluid flow is thus of relevance for volcanic eruption and gas emission modelling. We report here on nine discontinuity-bearing andesite blocks collected from Volcán de Colima, Mexico. We present a systematic porosity and permeability study of fifty cores obtained from the blocks collected, and interpret the genetic processes of the discontinuities through detailed microstructural examination. Bands in pumiceous blocks were inferred to be relicts of inhomogeneous bubble expansion which, despite significantly increasing porosity, do not markedly affect permeability. Other discontinuities in our blocks are interpreted to be shear strain-induced flow banding, cavitation porosity, and/or variably healed fractures. In each of these cases, an increase in permeability (up to around three orders of magnitude) was measured relative to the host material. A final sample contained a band of lower porosity than the host rock, characterised by variably infilled pores. In this case, the band was an order of magnitude less

permeable than the host rock, highlighting the complex interplay between dilatant and densifying processes in magma. We therefore present evidence for significant permeability anisotropy within the conduit and/ or dome of a volcanic system. We suggest that the abundance and distribution of strain localisation features will influence the escape or entrapment of volatiles and therefore the evolution of pore pressure within active volcanic systems. Using a simple upscaling model, we illustrate the relative importance of permeable structures over different lengthscales. Strain localisation processes resulting in permeability anisotropy are likely to play an important role in the style, magnitude, and recurrence interval of volcanic eruptions.

Keywords

Volcán de Colima; permeability; porosity; conduit processes; heterogeneity; microstructure.

Highlights

- We present and discuss microstructure of a variety of heterogeneous andesites.
- We interpret a range of formation mechanisms corresponding to different conduit or dome processes.
- 50 measurements of permeability k and porosity ϕ show strong permeability anisotropy in magma.
- Some of the presented features act as effective pathways for fluid flow, whilst others act as barriers.
- We outline the implications of this permeability anisotropy for outgassing and volcanic activity.

1. Introduction

Terrestrial volcanism is the surface expression of buoyancy-driven ascent of magma through the Earth's crust. Throughout its journey from depth to the surface, processes such as decompression (*e.g.* Proussevitch and Sahagian, 1998) and thermal vesiculation (Lavallée *et al*., 2015) force the exsolution (degassing) of magmatic volatiles such as H_2O and CO_2 (*e.g.* Li *et al.*, 2005). Whether through an interconnected bubble network in the magma (*e.g.* Eichelberger *et al.*, 1986; Okumura *et al.*, 2009), laterally into the edifice (*e.g.* Jaupart and Allègre, 1991; Jaupart, 1998; Collombet, 2009), or through fracture networks in magma, the edifice rock, and lava domes (*e.g.* Stasiuk *et al.*, 1996; Gonnermann and Manga, 2003; Rust *et al.*, 2004; Edmonds and Herd, 2007; Castro *et al.*, 2012; Cabrera *et al.*, 2011; Lavallée *et al.*, 2013; Pallister *et al.*, 2013; Gaunt *et al.*, 2014), the capacity for gases to migrate in a volcanic system is thought to influence its explosive potential. Effective outgassing is predicted to lessen the explosive potential of a volcano by inhibiting the build-up of pore overpressures within magma, whereas the ascent of poorly outgassed magmas is generally assumed to culminate in catastrophic explosive eruptions (as discussed by many authors, *e.g.* Eichelberger *et al.* 1986; Woods and Koyaguchi 1994; Rust *et al.* 2004; Edmonds and Herd, 2007; Mueller *et al.* 2008; 2011; Nguyen *et al.* 2014; Castro *et al.* 2014; Okumura and Sasaki 2014; Gaunt *et al.* 2014). The genesis and longevity of outgassing pathways is thus expected to constitute a critical parameter dictating eruptive behaviour.

Magma is inherently heterogeneous. The physico-chemical properties of magma evolve in time and space due to a host of interrelated processes, such as crystallisation (*e.g.* Carricchi.*et al.*, 2007; Vona *et al.*, 2011; Chevrel *et al.*, 2013; 2015), vesiculation (*e.g.* Bagdassarov and Dingwell, 1992; Burgisser *et al.*, 2010; Okumura *et al.*, 2013), and chemical differentiation (*e.g.* Giordano *et al*., 2008). In turn these processes are affected by variations in shear stress and strain rates across the conduit (Papale, 1999; Gonnerman and Manga, 2003; Caricchi *et al.*, 2007) or during dome extrusion (*e.g.* Smith *et al.*, 2001; Buisson and Merle, 2002; Cashman *et al.*, 2008). Evidence for this variability is abundant in volcanic environments, where extruded material can show wide ranges in crystal size and assemblage (Cashman, 1992; Blundy *et al*., 2006) and porosity and pore diameter (Kueppers *et*

al., 2005; Mueller *et al.*, 2005; 2008; Shea *et al.*, 2010; Lavallée *et al.*, 2012; Farquharson *et al.*, 2015; Burgisser *et al.*, 2011), in turn influencing permeability and strength (*e.g.* Zhu *et al.*, 2011; Kolzenburg *et al.*, 2012; Kendrick *et al.*, 2013; Farquharson *et al.*, 2015; Heap *et al.*, 2015a; Schaeffer *et al.*, 2015; Lavallée *et al.*, 2016). Magmas can also preserve discrete heterogeneities, evidence for strain localisation, in erupted material (*e.g.* Tuffen and Dingwell, 2005). Strain localisation processes in magma include extensional fracturing (*e.g.* Heiken *et al.*, 1988; Stasiuk *et al.*, 1996; Tuffen *et al.*, 2003; Tuffen and Dingwell, 2005; Castro *et al.*, 2014), frictional melting (*e.g.* Kendrick *et al.*, 2014a, b; Plail *et al.*, 2014), brecciation and gouge formation during shear fracturing (*e.g.* Pallister *et al.*, 2013; Cashman and Cashman 2006; Kennedy and Russell, 2012), cavitation (*e.g.* Smith *et al.*, 2001), and flow banding (*e.g.* Gonnerman and Manga, 2003; 2005).

Structural or textural discontinuities in porous media—especially where these heterogeneities are manifest as discrete tabular or (sub)planar features, such as stylolites and compaction bands—have often been observed to comprise conduits for or barriers to fluid flow, or more complex combined architectures (Caine *et al.*, 1996; Baud *et al.*, 2012; Lavallée *et al.*, 2013; Heap *et al.*, 2014c; Gaunt *et al.*, 2014; Deng *et al.*, 2015). The nature of these heterogeneities—their genesis, abundance, size (thickness and lateral extent), and orientation—can have a significant influence on the physical properties of the containing medium. For example, the scale and ratio of strain distribution and strain localisation in crustal fault zones has a marked effect on their permeability, resulting in four end-member regimes: localised conduits, localised barriers, distributed conduits, and combined conduit-barrier systems (*e.g.* Chester and Logan, 1986; Bruhn *et al.*, 1990; Caine *et al.*, 1996; Schultz and Fossen, 2008; Bense and Person, 2006). Due to the pre-established importance of fluid transport in volcanic systems, as well as the prevalence of preserved heterogeneities in erupted materials, it is of significance whether discontinuities in magma can in fact act as barriers to or conduits for fluid flow. To date there are few studies that explore the influence of magmatic heterogeneities on permeability, and even fewer that offer laboratory data. For example, Bouvet de Maisonneuve *et al.* (2009) present measurements on banded and non-banded pumice, showing that the former tend to be markedly less permeable in their dataset (by over an order of magnitude, depending on orientation). Cabrera *et al.*

(2011), Castro *et al.* (2012), and Berlo *et al.* (2013) discuss the permeability of rhyolite containing tuffisite (defined as fractures in magma or rock infilled with transported juvenile clasts and lithic fragments, *e.g.* Saubin *et al.*, 2016). Kolzenburg *et al.* (2012), Lavallée *et al*. (2016), and Kendrick *et al.* (2016) provide laboratory and field permeability measurements of andesite containing tuffisites and fractures. These studies conclude that the permeability of these features is—at least transiently—higher than that of the host rock mass, implying that they may serve as preferential routes for the outgassing of magmatic volatiles. Similarly, Gaunt *et al*. (2014) report a strong permeability anisotropy between the central and peripheral conduit of Mount St Helens volcano (USA) due to the juxtaposition of discrete lithofacies: a result of inhomogeneous ascent-driven strain localisation in the magma. Kendrick *et al*. (2014a) show that pseudotachylytes (frictional melts) from Soufrière Hills volcano (Montserrat) are notably less porous and permeable relative to the host rock and therefore may act as barriers to fluid flow in volcanic systems.

This study comprises a systematic examination of the porosity and permeability of discontinuity-bearing andesites to determine whether they comprise effective pathways for—or indeed barriers to—fluid flow in a volcanic system. We first show and describe nine discontinuity-bearing andesite blocks collected during a recent field campaign (May - June 2014) at Volcán de Colima (Mexico). We display the array of observed microstructures corresponding to these features, before outlining some potential mechanisms for their genesis. The influence of these discontinuities on the physical rock properties is then shown, and the attendant implications for volcanic activity, modelling, and field interpretations are outlined. The dataset of this study complements the large pool of data previously obtained on rocks from Volcán de Colima without discontinuities (*e.g.* Mueller, 2006; Kolzenburg *et al*., 2012; Lavallée *et al.*, 2012; Kendrick *et al*., 2013; Richard *et al*., 2013; Heap *et al*., 2014a; Farquharson *et al*., 2015; Lavallée *et al*., 2016).

2. *Case study: Volcán de Colima*

Volcán de Colima, located at the western margin of the Trans-Mexican Volcanic Belt (Figure 1a), is an active andesitic stratovolcano displaying a range of eruptive styles. Activity at the volcano underwent a significant increase from 1998, with two eruptive periods being defined: 1998 – 2011 and 2013 – current. During these eruptions, periods of lava flow emission and dome extrusion have been typically interspersed with cycles of explosive activity (Varley *et al.*, 2010; James and Varley, 2012; Lavallée *et al.*, 2012). A longer term cycle has been identified culminating in larger-scale sub-Plinian or Plinian events approximately once every century (Luhr, 2002). At the time of writing, Volcán de Colima had recently produced its largest pyroclastic density current (PDC) since the last catastrophic event in 1913 (Capra *et al*., 2015). During 10 - 11 July 2015, a significant increase in the effusion rate promoted a partial collapse of the growing dome, along with a portion of the crater rim on two occasions. A PDC, resulting from this activity, travelled down the Montregrande ravine and reached a distance of 10.7 km from the volcano summit. Widespread ashfall and the possibility of further pyroclastic density currents and lahars prompted the evacuation of a number of communities in the surrounding area, as well as a pre-emptive cessation of air traffic from Colima airport (Coordinación Nacional de Protección Civil, 2015a, b). In February 2016, an overflight of the volcano confirmed that a new lava dome is growing within the summit crater, signalling renewed effusive activity.

The rocks erupted since 1998 have been remarkably homogeneous in terms of their chemical composition, being andesitic with a SiO_2 content typically between 58 and 61 wt. % (*e.g.* Reubi and Blundy, 2008; Savov *et al*., 2008). Despite its petrographic constancy, the recent eruptive diversity of Volcán de Colima has given rise to a broad array of erupted material: field studies (Mueller*,* 2006; Farquharson *et al.*, 2015; Lavallée *et al.*, 2016) have found porosities of edifice-forming material to range between 0.02 and 0.73 (*i.e.* 2 and 73%). Similarly, the permeability of this material has been observed to differ by up to four orders of magnitude for any given porosity, and almost seven orders of magnitude over the whole dataset (Mueller, 2006; Kolzenburg *et al.*, 2012; Kendrick *et al.*, 2013; Richard *et al.*, 2013; Heap *et al.*, 2014a; Farquharson *et al.*, 2015). During a recent field campaign (May - June 2014), discontinuity-bearing rocks were collected from three sample sites (shown in

Figure 1a): two debris-flow tracks on the southwest and south flanks of the volcano (La Lumbre and Montegrande respectively), and the flanks of the parasitic vent Volcancito (Figure 1b).

3. *Materials and methods*

Nine blocks were sampled from the sites shown in Figure 1a. These blocks were collected so as to represent a variety of observable planar and subplanar heterogeneities (although this range is not necessarily exhaustive with respect to the features discernible in the field). While we cannot offer a quantitative assessment of the abundance of these various features, we highlight that they were commonly observable at each of the sampling sites and elsewhere on the volcano. We also draw attention to the fact that the sites marked in Figure 1a correspond to the final location of each block after emplacement and potential remobilisation. As such, we cannot draw specific inferences as to their origin based on the sampling location. Furthermore, we acknowledge that this sampling method means that neither the *in situ* orientation of the blocks nor their emplacement conditions—*i.e.* extrusion rate, style of activity etc.—can be assessed. The blocks collected for the purposes of this study were generally smaller than 300 mm in length, but we highlight that similar discontinuities can be seen on a metre scale. The nine blocks are shown and described in Figure 2 and Table 1, respectively.

Cylindrical core samples with a diameter of 20 mm were prepared from each block and precision-ground so that their end faces are flat and parallel. The length of each core (from 25 to 40 mm) was dependent on the initial block size. The length to width ratio of our samples was therefore greater than one in each case (length to width ratios lower than one are not recommended for laboratory permeability measurements). Where possible, cores were extracted such that the feature of interest was either parallel or perpendicular to the core axis (*i.e.* in the y and z directions, respectively: Figure 3a). Again where possible, additional cores of the host rock were obtained so as not to include the feature of interest. Altogether, 50 samples were prepared from the nine initial blocks (shown in

Appendix A). All subsequent measurements were performed after the cores had been oven-dried at 40 °C under a vacuum for a minimum of 48 hours.

Connected gas porosity (ϕ) was determined using helium pycnometry (AccuPyc II 1340 from Micromeritics). Gas permeability k was measured under 1 MPa of confining pressure using a steady-state benchtop permeameter, with nitrogen gas as the permeant. While we appreciate that measurement under a low confining pressure may not necessarily represent the *in situ* conditions, one must note that imposing higher pressure requires presupposing a depth of origin for each sample. Similarly, while room-temperature experiments may not capture additional complexities of fluid migration in high-temperature conduit magma, attempting to account for this in the experimental design means presuming a single elevated temperature at which to measure permeability. Importantly, the imposed experimental conditions (fixed pressure and temperature) allow us to compare the permeability of the different samples measured in this study. A schematic of the permeameter is shown in Figure 3b and a close-up of the coreholder setup in Figure 3c. The volumetric flow rate was measured at a range of pressure differentials across the sample (∇P: between 0.001 and 0.2 MPa), to assess the need for correction due to inertial effects (*i.e.* non-Darcian flow). Where necessary, Forchheimer (1901) or Klinkenberg (1941) corrections were applied to the apparent (measured) permeability to derive the permeability of the samples. Thin sections of all but one of the samples were also prepared in order to explore and analyse the microstructure using a Scanning Electron Microscope (SEM); due to the similarity of the two pumiceous samples, COL-V-1 and COL-V-6 (Table 1; Figure 2a, b), the microstructure was only examined for the latter (both blocks were collected from the same fall deposit; as such we deem it probable that the macroscopically similar banding in these samples is characteristic of the same genetic process, rather than two separate mechanisms being coincident in the same deposit). Digital image analysis of photomicrographs was performed in order to estimate 2D porosities both inside and outside of the features using the open-source image-processing program ImageJ (see Schneider *et al.*, 2012). For select samples, X-ray Fluorescence (XRF) was used to assess compositional differences between the band and the corresponding host rock.

4. *Microstructural observations*

This section outlines microtextural and microstructural observations of each sample. We also provide image-derived 2D porosities (see Table 2). Inferred genetic processes—based on our observations—are discussed in a later section.

Block COL-V-6 is a pumiceous block made up of distinct dark and light grey portions (Figure 2a; Figure 4a - c). The 2D porosity is around 0.23 in the dark grey portion, and approximately 0.50 in the lighter coloured regions (Table 2). In the less porous dark grey portions, pores are often equant and typically around 50 μm in diameter, but can be 50 - 100 μm (Figure 4a, b). In the lighter coloured, (*i.e.* more porous) regions, pore diameters are typically larger—generally around 100 μm, and occasionally up to 500 μm—and are often non-equant (Figure 4c). The long axis of pores in the lighter coloured material is preferentially oriented perpendicular to the interface between the layers, with these pores (the 100 μm range) having an aspect ratio of approximately 2:1. This is in contrast to the pores in the darker coloured portion, which show a preferable orientation parallel to this interface (although this tendency is much less pronounced). The boundary between the light grey and dark grey regions is sharp. We also observe occasional jigsaw-fit broken crystals (Figure 4b).

Block COL-V-5 (Figure 2c; Figure 4d-f) is made up of distinct light grey and dark grey portions. Both regions contain microcracks, and porosity is equivalent in both the lighter and darker coloured parts of the block ($\phi = 0.09$ in each case: Table 2). In the light grey region, pores are generally from 10 - 100 μm in diameter and are usually rounded (Figure 4e). In contrast, pores in the dark grey region tend to be smaller in size (between 10 and 50 μm) and amœboid—rounded but highly irregular—in shape (Figure 4f). We thus infer that the difference in colour is due to the contrasting pore size and pore size distribution, rather than a significant difference in porosity. The boundary between these two portions is difficult to distinguish on the microscale (as evidenced by the low-magnification SEM image shown in Figure 4d). Microstructural examination of the interface indicates that the transition

between regions dominated by different pore sizes (and shapes) occurs over ~2000 μm. We also note the presence of cm-size xenoliths within the sample.

Block COL-V-3 contains tapered bands or lenses ($\phi = 0.29$) up to approximately 500 μm in width within a dense host rock ($\phi = 0.01$) (Figures 4g and 4h). The dense host rock contains pores, generally less than 10 μm in diameter, and microcracks (Figure 4h). The relatively higher porosity in the bands is responsible for their paler colour relative to the host material. The transition between the host rock and the more porous bands occurs over about 100 μm in each case (Figure 4h). The bands consist of variably sized (from 50-100 microns down to less than 10 microns) angular particles with varying sphericity (for example, we note the presence of abundant platy or needle-shaped particles). Consequently, the inter-granular porosity is irregularly shaped (Figure 4i). Throughout the host material, we observe micro-scale crystallites within the glassy groundmass; this texture—the so-called "feathery" texture of Horwell *et al.* (2012; 2013)—is shown in more detail and discussed in Section 5.4.

The host rock of block COL-V-4 is glassy and low-porosity ($\phi \approx 0.06$). As well as microcracks, the porosity of the host rock is made up of subequant pores that tend to be in the region of 10 - 50 μm in diameter (Figure 4j), although some are as large as 300 μm. The host rock contains a number of slightly anastomosing porous bands, from 1 mm up to 10s of mm in thickness, containing a porosity of around 0.32 (Table 2, Figure 4j-l). Thus the relatively higher porosity within the band makes it appear lighter in colour relative to the dense surrounding rock. There is a sharp contact between the host rock and the band, occurring over a few tens of microns. The interior structure of the band ranges from zones of subangular, granular material at the margins (characterised by a particle size rather than a pore size: particles are generally around 20 μm diameter), to more coherent material towards the centre of the band containing rounded, amœboid pores, which are generally on the order of 10 to 50 μm in diameter (Figure 4k, l). There are also large *en échelon* tensional fractures (~50 μm wide and ~400 μm in length) which cut through the band, oriented approximately 45° to the band (Figure 4k),

and can be seen to skirt around crystal boundaries. Within the granular margins of the band, there are also patches of coherent material, typically adjacent to large phenocrysts (Figure 4k).

Three bands can be discerned in block COL-M-1, each approximately 5 mm in width (Figure 2f), two of which are shown in Figure 4m. The heavily microcracked host rock contains a porosity of 0.01, in contrast to the bands which have a porosity of around 0.20. Accordingly, the bands appear paler in colour than the host rock. We also observe feathery groundmass textures (see Horwell *et al.*, 2012; 2013) in the host rock as well as crystalline silica, darker in colour than the groundmass (discussed further in Section 5.4). Porosity inside the bands tends to be highly irregular in shape (Figure 4n). One population of pores is evident in the range of 10 - 50 μm in diameter, with other, larger pores (100s of μm in diameter) occurring adjacent to large rigid crystals (Figure 4n, o). Despite the bands being very tabular, the transition between each band and the host rock tends to be relatively diffuse, occurring over a distance of approximately 500 μm (Figure 4n, o).

COL-L-1 is a dense glassy block (with a host rock porosity of approximately 0.03) containing tabular bands with relatively higher porosity (around 0.10), manifest in the difference in colour observable in the hand sample. The porosity of the host rock typically comprises small pores (< 20 μm in diameter) and microcracks (Figure 4p-q). The material inside the bands is made up of subangular, prolate fragments with their long axes generally < 50 μm in length, interspersed with relatively large phenocrysts up to 500 μm in diameter (Figure 4q-r). We also note dark patches of cracked crystalline silica. The transition between host and band occurs over a width of up to 1 mm (Figure 4q).

COL-L-2 is another dense, glassy block (with a host rock porosity of approximately 0.01) containing a 3 - 5 mm-thick tabular band containing a porosity around 0.18 (Figure 4s) (the high-porosity band is correspondingly lighter in colour than the rest of the sample). The shape of the intergranular porosity within the band is amœboid, typically 100 μm or less in diameter, but occasionally up to around 200 μm (Figure 4t-u), whereas the porosity in the host rock consists of equant pores no greater than 100 μm in diameter, and abundant microcracks. Notably, the band appears to deflect around a xenolith in

the host material (Figure 4s, inset). There is a discrete interface between the host rock and the porous band (Figure 4t-u). Throughout the groundmass, we observe acicular lath-like crystals, darker than the rest of the groundmass constituents (discussed further in Section 5.4).

Finally, COL-L-4 is a block with a host rock porosity around 0.13; the porosity of the host rock is made up of irregularly-shaped pores—from around 100 to 1000 μm in diameter—and abundant tortuous microcracks. The band visible in the block (Figure 2i, Figure 4v inset) is characterised by a region of relatively lower porosity ($\phi \approx 0.03$). Much of the band appears reddish in colour at hand-sample scale, as well as in the prepared thin section. The inner walls of the pores at the margins of the low-porosity band are defined by numerous high aspect ratio (platy or needle-like) crystals. Towards the interior of the band, the porosity is characterised by the interparticulate space between this platy or needle-like material (Figure 4w, x), or spherical pores containing variably granular, angular to rounded particles from 10 - 50 μm in diameter (Figure 4w). In the centre of the bands, porosity exists as ~200 μm-diameter patches of subrounded pores that are generally < 20 μm in diameter. The boundary between the host rock and the relatively lower porosity band is very diffuse (the band is difficult to discern on the microscale, Figure 4v), occurring over around 2000 μm in some areas.

5. *Microstructural interpretations*

The various features described above provide snapshots of a range of interrelated conduit or dome processes. However, the microstructures that develop due to any given process may well overprint earlier textures. To add further complication, the extent of expression of any specific texture is likely to depend heavily on the time allowed for the responsible mechanism to operate. As such, we do not ascribe any one definitive genesis to the features discussed in this study but refer to the microstructure to bolster the interpretations we regard as most likely in each instance.

5.1 Banding in pumiceous samples

XRF analysis of a banded pumiceous block (COL-V-1: Figure 2a) indicates that there is a negligible difference in bulk composition (of the major and trace elements analysed) inside and outside of the bands, suggesting a predominantly physical process in their genesis. This is in contrast to a number of other studies which discuss banding in pumice—for example Vezneky and Rutherford (1997), Hall *et al.* (1999), and Bouvet de Maisonneuve *et al.* (2009)—which attribute observed heterogeneities to the intermingling of magma batches of distinct composition or variations in magma differentiation. Burgisser *et al.* (2010) show macroscopically similar banded pumice collected at Soufrière Hills Volcano, Montserrat, ascribing the heterogeneity of porosity within individual samples to corresponding variations in water content. Based on our porosity data and microstructural observations (notably, band-perpendicular bubble elongation: Figure 4b), we surmise that the constituent material underwent a certain degree of extension or decompression-driven bubble expansion assisted by viscous deformation (*i.e.* above its glass transition *T*g), but not to a degree sufficient to wholly fragment the sample. This process has been observed in shock-tube experiments (*e.g.* Martel *et al.*, 2000; Namiki and Manga, 2005), which demonstrate that decompression can cause volatile exsolution from a supersaturated liquid, followed by bubble growth and coalescence.

Band-parallel elongation of pores in the denser material (Figure 4b) may be indicative of coincident compression associated with the propagation of a rarefaction wave (*i.e.* pure-shear flattening of neighbouring bubbles during bubble expansion: Wright and Weinberg, 2009); however we can infer that the process was rapid and predominantly extensional as we observe evidence of crystal parting at the band-host rock interface (Figure 4c). Comparable breakage of crystals was reported by Kennedy *et al.* (2005), who attribute similar bands in pumice to lateral conduit implosion following the propagation of a fragmentation front through the magmatic column. Such textures could conceivably also arise during magma ascent in the conduit, or during phases of lava dome-extrusion: structures that are inherently prone to collapse and depressurisation (*e.g.* Fink and Kieffer, 1993; Navon *et al.*,

1998; Voight *et al.*, 2006). Indeed, variably-vesiculated layers of pumice and glass observed at Inyo Dome and Big Glass Mountain, both in the USA, illustrate the complex textural heterogeneities that can develop due to dome depressurisation (Fink and Manley, 1987; Castro *et al.*, 2005).

5.2 Shear strain-induced flow banding

The development of laminar flow due to vertical and horizontal gradients in temperature, pressure, and shearing mode or internal friction (*e.g.* Denlinger and Hoblitt, 1999; Mastin, 2002; Rust and Manga, 2002; Rust *et al*., 2003; Gonnerman and Manga, 2005; 2007) can ultimately partition magma properties such as crystal content, water content, or porosity, resulting in heterogeneous deformation of the magma even over microscopic scales (*e.g.* Wright and Weinberg, 2009; Laumonier *et al.*, 2011; Lavallée *et al.*, 2013). Plug or piston flow within a magma conduit (*e.g.* Gonnerman and Manga, 2003; Hale and Mülhaus, 2007) dictates that shear strain in magma should be higher at the periphery of the conduit than in the centre (the effect of a variable stress profile across a conduit on a non-Newtonian magma rheology containing crystals and bubbles favours strain localisation, and in particular simple shear, in regions of highest strain rate near the conduit margin; Lavallée *et al*., 2007; Dingwell *et al.*, 2015). Similarly, large strains—and large gradients thereof—have been estimated from actively extruding domes (*e.g.* Cashman *et al.*, 2008), and are expected to be prevalent in dome- and spine-building systems (*e.g.* Griffiths and Fink, 1993; Buisson and Merle, 2004; Hornby *et al.*, 2015). Moreover, additional stresses are likely to be pervasive within an active volcanic system, for example due to cumulative edifice construction and loading of the basement (*e.g.* de Vries and Borgia, 1996; de Vries and Merle, 1998; Gerst and Savage, 2004; Roman *et al.*, 2004; Odbert *et al.*, 2015). Deformation induced solely by simple shear (which is to say an isochoric or isovolumetric process) would not result in the creation or destruction of porosity (*i.e.* dilation or densification of the magma), but in inhomogeneous deformation of the porous melt and modification of the permeability (Wright *et al.*, 2006). This is in line with our observations of sample COL-V-5 (Figure 2c, Figure 4d-f): while the pore size distribution is notably different between the competent light and dark grey regions, the connected porosity is equivalent in both (~0.09: see Table 2). Further, the inclusion of

xenoliths in the block may be indicative that energetic shearing has occurred (Rust *et al.*, 2004). This interpretation is given weight by the fact that XRF analysis of this sample yields comparable bulk composition in both the light grey and dark grey portions, suggesting a predominantly physical process rather than a compositional one. Nevertheless, alternative physical mechanisms cannot be discounted. For example, finite element modelling of shallow-vent exogenous dome growth predicts the concurrence of magma batches with contrasting degassing histories, manifest in juxtaposed regions of differing porosity (Massol and Jaupart, 2009).

Purely laminar flow in a conduit is, however, not necessarily the norm (Costa and Macedonio, 2003). Rather, some degree of volumetric change may be associated with shear strain, resulting either in transtension (shear and extension) or transpression (shear and compression). Viscous-to-brittle transtension of fluid—whereby the vapour phase of a liquid is formed due to a local pressure or stress differential—is also termed cavitation (*e.g.* Gruzdkov and Petrov, 2008), and potential evidence for this process exists in the microstructure of, for example, COL-V-4, COL-M-1, and COL-L-1. Below, we describe some of these characteristic features—shown in more detail in Figure 5—analogous to those often observed in material science (such as ceramics studies: Chokshi, 1997), and texturally similar to those described in dacitic dome rocks from Unzen, Yakedake, and Daisen volcanoes (all in Japan) by Smith *et al.* (2001). For example, *en échelon* extensional porosity can be seen within some of the porous bands, as shown in Figure 5a (COL-V-4; see also Figure 4j, k). These high aspect ratio pores skirt crystal boundaries, comparable to the "crack-like" porosity of Smith *et al.* (2001). We further note that these features are comparable in form and formation to experimentally-created "tension gashes" in pure melts (A. Kushnir, pers. comm.) and extensional fracturing in crystalline magma under uniaxial compression (Lavallée *et al.*, 2013). Moreover, Figure 5b (COL-M-1) and Figure 5c (COL-V-4) show where porosity has preferentially developed along the borders of large phenocrysts, which can be interpreted as further evidence of cavitational porosity (this can also be observed in sample Col-L-1: see Figure 4q, r). Notably, Figure 5c shows a tail of low-porosity adjacent to a phenocryst. Although the *in situ* stress field cannot be known, we interpret this feature as

an indicator of localised differences in the stress field—*i.e.* a pressure/stress shadow—which is a prerequisite condition for cavitation.

5.3 Magma fracture and sintering

Brittle behaviour in magma is typically ascribed one of two mechanisms: magma fragmentation resulting from a pore pressure that exceeds the tensile strength of the magma (*i.e.* a fragmentation threshold: *e.g.* Alidibirov and Dingwell, 1996; Zhang, 1999; Koyaguchi *et al.*, 2008), or magma failure due to rapid shearing surpassing a critical strain rate in areas of strain localisation (*e.g.* Woods and Koyaguchi, 1994; Martí *et al.*, 1999; Papale, 1999; Gonnermann and Manga, 2003; Melnik *et al.*, 2005; Lavallée *et al.*, 2008; 2013). In both cases, failure occurs at the glass transition because the strain rate cannot be relaxed viscously and exceeds the elastic limit of the material (Dingwell, 1996). The former process is associated with relatively rapid magma decompression (as outlined in section 5.1) or gas waves or slugs fluxing through the magmatic column (*e.g.* Michaut *et al.*, 2013). As for the latter, a critical strain rate criterion may be met at any depth in the conduit or within extruding lava domes, resulting in magma fracture (as discussed by, *e.g.* Dingwell, 1996; Papale, 1999; Webb and Dingwell, 1990; Tuffen *et al.*, 2003; Edmonds and Herd, 2007; Lavallée *et al.*, 2008; Tuffen *et al.*, 2008; Cordonnier *et al.*, 2012), if the melt viscosity prevents sufficient stress relaxation during rapid magma ascent (Goto, 1999; Papale, 1999; Gonnerman and Manga, 2003).

The sharp transition we observe between the host material and the bands present in many of our samples (COL-V-3, COL-L-2, COL-V-4), hints at brittle failure of the magma. Examples of the well-defined contact are shown in Figure 6a and 6f. In each of these cases, these fractures are also filled with variably granular material, as we may expect if ash-sized material is generated on the fault plane or transported through the fracture. Once a fracture is generated in rock or magma, the conditions may exist to allow subsequent viscous sintering or hot pressing of fragmental material within the fracture (*e.g.* Stasiuk *et al.*, 1996; Tuffen *et al.*, 2003; Kolzenburg *et al.*, 2012; Vasseur *et al.*, 2013; Wadsworth *et al.*, 2013; Heap *et al.*, 2014a; 2015c), either *in situ* or after some degree of

transportation (Tuffen and Dingwell, 2005). Viscous sintering—the agglutination of melt particles above their glass transition temperature—is common in a range of volcanic environments, examples of which include rhyolitic dykes and conduits (*e.g.* Tuffen *et al.*, 2003; Tuffen and Dingwell, 2005; Okumura and Sasaki, 2014), welded block-and-ash flow deposits (*e.g.* Michol *et al.*, 2008; Andrews *et al.*, 2014; Heap *et al.*, 2014a), lava spatter and spatter ramparts (*e.g.* Mellors and Sparks, 1991; Sánchez *et al.*, 2012), localised agglutination of scoria (Wadsworth *et al.*, 2015), conduit-filling pyroclastic material (*e.g.* Kolzenburg and Russell, 2014), and rheomorphic and lava-like ignimbrites (Branney *et al.*, 1992; Lavallée *et al.*, 2015). More specifically, the sintering of "transiently granular" material (Wadsworth *et al.*, 2014) has been described in terms of fracture healing in magma (*e.g.* Tuffen *et al.*, 2003; Heap *et al.*, 2015c). Viscous sintering of volcanic material requires the temperature and the timescale of the process to be such that the material remains in a liquid regime (above the glass transition *T*g of its melt phase), whereupon the melt structure can relax and heal particulate material via diffusion (*e.g.* Vasseur *et al.*, 2013). The process encompasses three separate stages (*e.g.* Vasseur *et al.*, 2013; Wadsworth *et al.*, 2014): (1) point-to-point connection of melt "necks" between granular materials (incipient sintering or welding), (2) a variably porous but melt-dominated medium (partial sintering or welding) and, (3) a nonporous melt and crystal phase (*i.e.* fully sintered or welded).

Microstructural evidence of the first two of these stages can be observed in a number of our samples, examples of which are shown in Figure 6. Discrete angular granular material is typically observed at the inner margins of fractures (Figure 6c, 6h). Advancing towards the centre of each sintered band (*i.e.* from Figure 6c → e and Figure 6h → j), we observe that fragments are progressively more rounded, and often connected by necks of glassy groundmass, indicating melt relaxation associated with incipient to partial sintering. This process is reflected in increasingly connected groundmass and correspondingly isolated porosity, as the material transitions from fragments within void space to a porous melt wherein the original angular nature of the fractures cannot be discerned. Pores also appear increasingly spherical or amœboid within the centre of either band (Figure 6e, 6j), illustrative of the relaxation of the internal surface area of the porosity with ongoing sintering (*e.g.* Mackenzie

and Shuttleworth, 1949; Wadsworth *et al.*, 2014). Comparison of samples Col-V-4 and Col-L-2 (Figure 6a - e; Figure 6f - j) illustrates that these sintering textures are generally more developed in the latter sample, suggestive of higher temperatures or greater depths (*e.g.* Wadsworth *et al.*, 2014; Heap *et al*., 2015c), or longer timescales (Vasseur *et al*., 2013). Thus we can observe differing degrees of sintering both within a single fracture and between different samples.

5.4 Evidence for gas transport

The low-porosity band within the sample COL-L-4 (Figures 2i and 4v-x) shows pores partially filled with variably-sintered fragmental material (Figure 7a; Table 2). Based on our observations we speculate that the progressive pore infilling is the result of ash deposition from circulating hot ash-laden fluids. The hot and "sticky" ash particles first adhere to and coat the pore walls (as in Figure 7b), subsequently reducing pore throat apertures, which may well encourage further agglutination and filling of the pores (Figure 7c). The originally angular and fragmental ash particles (Figure 7a) gradually lose their shape as surface tension reduces the curvature of the melt/fluid interface, promoting the rounding of particles (Figure 7b, c; see Vasseur *et al.*, 2013). Eventually the pore becomes completely filled and the particles continue to densify through sintering. At this stage, the characteristics of the original granular material and the original pore are mostly eradicated; however, relics of the originally granular material are defined by remnant microporous patches (Figure 7d, and inset).

Other than in sample COL-L-4, we do not observe definitive evidence for the transport of fragmented magma or fault gouge—whether juvenile or from previous explosive activity—in our samples. Nevertheless, recent studies (Kolzenburg *et al*., 2012; Kendrick *et al*., 2016; Lavallée *et al*., 2016) suggest that this process may be common at Volcán de Colima in materials derived from either the dome or conduit. However, we do observe variable oxidation of the bands in some hand samples (COL-V-4, COL-L-4: see Table 1), indicative of through-flow of hot magmatic fluids. This is in

agreement with the findings of Plail *et al.* (2014), who interpreted changes in metal compositions in banded volcanic rock as a result of magmatic gas flow.

Further, textural evidence of silica polymorphs, both within bands and in the host rock groundmass, may point to transport of magmatic volatiles through porous discontinuities. Figure 8a shows sample COL-M-1, highlighting the darker-coloured crystalline silica. The diagnostic "fish-scale" microcracking texture is indicative of cristobalite having undergone the β- to α-cristobalite transition (*e.g.* Damby *et al.*, 2014), often observed in volcanic dome rocks from, for example, Inyo Domes, USA (*e.g.* Swanson *et al.*, 1989), Mount St Helens, USA (*e.g.* Blundy and Cashman, 2001), and Gunung Merapi, Indonesia (*e.g.* Kushnir *et al.*, 2016). In sample COL-L-2 (Figure 8b) we observe lath-like crystals we interpret to be tridymite (see Blundy and Cashman, 2001). Figure 8c shows an example of a sample exhibiting a feathery groundmass texture (sample COL-V-3), characterised by microscale crystallites occurring within the groundmass glass. The growth of this texture is thought to represent variable devitrification of the initially glassy groundmass (Horwell *et al.*, 2012; 2013). We also observe needle-like or platy textures within pores and bands of some samples, an example of which is shown in Figure 8d (sample COL-L-4). These textures are consistent with prismatic cristobalite growth observed in lavas from the dome of Soufrière Hills volcano (Montserrat) by Horwell *et al.* (2013), both in terms of form and tendency to occur within pores and fractures in the rock. These authors interpret the latter fact as evidence for vapour-phase mineralisation.

Vapour-phase crystallisation of silica polymorphs, namely tridymite and cristobalite, provides strong evidence that transiently connected porosity (*e.g.* cavities or discrete fractures in magma) does indeed serve as a transport network for element-rich magmatic gases. Tridymite and cristobalite are metastable at high temperatures and low pressures (*e.g.* Deer *et al.*, 1996; Damby *et al.*, 2014), indicating that the processes involved in forming or infilling these fractures and pores must be occurring in relatively shallow regions of the dome or conduit. This is in agreement with the findings of Ball *et al.* (2015), who suggest that hydrothermal alteration and precipitation will be preponderant

in talus-mantled lava domes, where these processes are enhanced due to favourable heat and permeability conditions.

Similarly, Cashman *et al*. (2008) show evidence of tridymite in dacite from Mount St Helens (USA), and estimate that its presence necessitates relatively low pressures (between around 5 and 25 MPa). The observation that porosity is created and destroyed by physical and chemical processes in the upper conduit and surficial dome emphasises the importance of understanding localised spatio-temporal variations in permeability.

6. Permeability anisotropy

Our measurements, and the attendant discussion in the previous section, highlight that various conduit and dome processes manifest themselves differently: they may increase or decrease porosity, or porosity can remain effectively constant. The following section discusses the consequent influence on the permeability of these discontinuity-bearing samples, which can be distinguished into four main categories: (1) an increase in porosity may exert only a negligible influence on permeability, (2) an increase in permeability may arise even when porosity is essentially unchanged, (3) an increase in porosity can be accompanied by an increase in permeability, or (4) a decrease in porosity can yield a decrease in permeability.

In the majority of the collected blocks, porosity within the band or fracture is higher than or equivalent to that of the host rock mass (Table 2). The exceptions are the banded pumiceous samples (COL-V-6 and COL-V-1: Figure 2a, b, Figure 4a-c) and sample COL-L-4 (Figure 2i, Figure 4v-x). The 2D porosity data derived from SEM photomicrographs (Table 2) agree with the connected gas porosity measurements performed on cylindrical cores obtained from each block (Table 3). Gas permeability of all core samples are also given in Table 3, where we also indicate whether the heterogeneity—if present—was parallel or perpendicular to the core axis (hence the direction of fluid flow). Permeability as a function of porosity is shown in Figure 9. In general, high porosities are

associated with high permeabilities, and low porosities with low permeabilities, although the precise relation differs between the high (>0.30) and low (<0.20) porosities (as similarly commented on by Heap *et al.*, 2014a; Farquharson *et al.*, 2015; Kushnir *et al*., 2016).

The permeability of a heterogeneous porous medium is termed here the "equivalent" permeability k_e (see Renard and De Marsily, 1997 for a review). For sample sets where we have at least one core containing a band parallel to the core axis, and at least one band-free core, we are able to decouple the equivalent permeability in order to estimate the permeability of the band or fracture itself via a simple two-dimensional parallel-plane model. We assume that the ("intact") host permeability k_i is that of the feature-free core; thus the permeability of the band or fracture k_f is calculated as a function of the sample area A_s, the band area A_f, and the host and equivalent permeabilities, such that

$$k_f = \frac{k_e A_s - k_i(A_s - A_f)}{A_f} \quad (1).$$

This method has previously been used to calculate the permeability of tensile fractures in variably-porous andesites from Ruapehu (New Zealand) (Heap and Kennedy, 2016). Note that this model assumes that A_f is small compared to A_s. Table 4 gives the parameters used, as well as the mean band or fracture permeabilities, for each of the rocks where this calculation was possible. Further, we show the "relative" permeability k_r between the host rock and the discontinuity, given here by the fractional change in permeability with respect to the host value

$$k_r = \left(\frac{k_f - k_i}{k_i}\right) \quad (2),$$

where a positive value means that a feature is more permeable than its corresponding host rock, while a negative value indicates the reverse. The data of Tables 3 and 4 show that the presence and orientation of a discontinuity has a variable influence on the permeability of our samples: permeability can increase, decrease, or remain roughly constant depending on the properties of the host rock and the feature. These scenarios are discussed below.

We will first examine the banded pumice. Data presented in Figure 9b and Table 3 show that permeability of pumiceous material (COL-V-1 and COL-V-6) varies by less than an order of magnitude: despite ranging between ~0.35 and ~0.65 porosity, permeability ranges from 5.44×10^{-14} to 3.42×10^{-13} m^2 in these samples. As observed in previous studies (*e.g.* Farquharson *et al.*, 2015; Kennedy *et al*., 2015; Kushnir *et al*., 2016), the permeability-porosity relationship of porous volcanic rocks can be described by a relatively low power law exponent above a certain threshold in porosity. This is thought to be due to the fact that above this threshold effective fluid pathways (a so-called "backbone" of permeability) must—necessarily—already exist. Thus, a large increase in porosity by rapid bubble expansion, as inferred in section 5.1, is likely to be associated with only a marginal increase in permeability. Similarly, we may assume that pure-shear flattening of these bubbles will not significantly decrease permeability until a threshold level of compaction.

Sample COL-V-5 has been interpreted as preserving a simple shearing process. We note that the permeability of the darker coloured side (1.37×10^{-14} m^2) is measurably higher than that of the lighter coloured portion ($2.90 - 6.24 \times 10^{-14}$ m^2: Table 3; Figure 9a). Thus, in samples where the core axis is parallel to the discontinuity, the permeability is controlled by that of the most permeable region (on the order of 10^{-14} m^2). Conversely, when the core axis is perpendicular to the discontinuity, the permeability is comparable to the lower value, on the order of 10^{-16} m^2 (Figure 9a). As the fraction of connected porosity shows negligible variation, we hypothesise that the differences in permeability must be driven in this case by some other corresponding parameter. As noted previously, the pore size and pore size distribution differs between the relatively high- and low-permeability regions. In turn this presumably influences the mean aperture of fluid pathways, as well as other factors such as the relative tortuosity of each pathway. Local differences in the stressing history of the magma may therefore provide a partial explanation for the wide variability in volcanic rock permeability observed in nature (*e.g.* Mueller *et al*., 2005; 2006; Farquharson *et al*., 2015).

Many of the discontinuity-bearing samples discussed herein are considered to represent variably-sintered fractures. For one of these—sample COL-V-4 (Figure 4j-l)—we obtain fracture permeabilities

on the order of 1.0×10^{-13} m^2, approximately three orders of magnitude greater than the mean permeability of non-fractured cores of this sample (1.6×10^{-16} m^2). It is thus evident that these fractures comprise a highly efficient conduit for fluid flow, despite being partially healed (experiments suggest that the unhealed fracture permeability of a 20 mm-diameter sample containing one through-going fracture is in the vicinity of 10^{-11} m^2: Heap and Kennedy, 2016). This supports the inference of previous authors (*e.g.* Edmonds and Herd, 2007; Castro *et al.*, 2014), that magma fracture is an effective means of outgassing volatiles from conduit-dwelling magma. However, fractures observed in some of our other samples show evidence of more mature sintering (summarised in Figure 6f - j), and are inferred to originate from greater depths or suggest longer healing timescales. It has been previously suggested through modelling that sintering timescales decrease with depth due to the correspondingly high magmastatic (and lithostatic) pressure and low effective viscosity (Russell and Quane, 2005; Quane *et al*., 2009; Heap *et al*., 2015c). However, it has been noted that volatile resorption at low pressures may actually serve to accelerate viscous sintering (Sparks *et al.*, 1999) by locally reducing the melt viscosity (Hess and Dingwell, 1996). Viscous sintering results in densification and a reduction of the connectivity of the porous network (*e.g.* Vasseur *et al.*, 2013), and is commonly recorded in volcanic environments (*e.g.* Grunder and Russell, 2005; Quane *et al.*, 2009; Kolzenburg and Russell, 2014). This process correspondingly reduces permeability (Heap *et al.* 2015c; Wadsworth *et al.*, 2016), ultimately tantamount to the destruction of fluid pathways in magma.

The infilled and relatively low-porosity band of sample COL-L-4 (Figure 4v-x; Figure 7), yields a fracture permeability of 6.7×10^{-14} m^2, approximately an order of magnitude lower than that of the surrounding rock mass (2.4×10^{-13} m^2); correspondingly the relative permeability k_r is negative (Table 4). To preferentially permit the passage of hot ash-laden fluids (as discussed in Section 5.4), this now low-porosity band used to be, in all likelihood, a band of higher porosity and permeability than the surrounding host rock. Although the preserved features studied herein only provide snapshots of dynamic processes, this indicates a strong time-dependence of permeability in magma: once a fracture is generated, fault gouge and preferentially transported fragmental material will quickly sinter due to their small size (*e.g.* Wadsworth *et al*., 2015). In turn, permeable fractures, cavities, or bubble

networks, may progressively decrease in permeability until they are of comparable or, in some instances, lower permeability than the original magma.

In summary, we typically observe that if a feature acts as a conduit for fluid flow, then orientation of the feature parallel to fluid flow has a markedly greater influence on permeability than when the feature is normal to fluid flow. On the other hand, a feature acting as a barrier for fluid flow will exert its maximum influence when oriented perpendicular to fluid flow. This is due to the difference between fluid flow in parallel and serial systems. Simply put, when offered the choice of parallel layers, fluid will preferentially flow through the layer that is most permeable, and the overall permeability is thus governed by the most permeable element. Contrastingly, in a serial system, fluids must flow through each and every layer, and permeability is thus controlled by the layer with lowest permeability.

7. Implications

7.1 Outgassing and volcanic activity

Figure 10 summarises the influence of processes discussed in the previous two sections. Magma fracture causes relatively large changes in magma permeability, over relatively small increments in porosity (Figure 10a). Indeed, our data suggest that permeability may increase by three orders of magnitude or more for a change in porosity of only around 0.03 or 0.04 (Table 3). Similarly, shear-induced transtension or cavitation of magma is predicted to yield a local increase in porosity and permeability (Figure 10a); our data for sample COL-M-1, for example, indicates that for comparable porosities (between 0.05 and 0.07), permeability of the magma can be increased by around two orders of magnitude if these porous discontinuities are preferentially oriented (Table 3; Figure 9a). By contrast, densifying processes—*e.g.* viscous sintering or transpression—result in decreases in both porosity and permeability (Figures 10b). Figure 10a and 10b further illustrate the contrasting

influences of bubble expansion and the collapse of foaming magma. Because the magma is already highly permeable—due to its high initial porosity—increases or decreases in porosity of tens of percentage points (*e.g.* from $\phi \approx 0.30$ to $\phi \approx 0.60$) are not expected to have a marked influence on the permeability of the magma (less than one order of magnitude difference).

It is important to note that—irrespective of the processes acting on the physical properties of a specific clast or unit of magma (Table 3; Figure 9)—we observe that the permeability-porosity relationship of heterogeneity-bearing rocks (and indeed, the permeability-porosity relationship of the features themselves) appear always to follow a trend remarkably similar to that of andesitic rock free of macroscopic heterogeneities (shown in Figure 10c). It follows that at low magma porosities (*i.e.* lower than around 0.15 or 0.20: see Figure 9a), permeability evolution is dominated by the generation and healing of fractures, just as in low-porosity volcanic rocks the permeability evolution is strongly governed by the generation or closure of microcracks (Vinciguerra *et al*., 2005; Nara *et al*., 2011; Heap *et al*., 2014a; Farquharson *et al*., 2015). At higher porosities, the influence of bubble growth, bubble coalescence, and expansion-driven fragmentation become dominant (Figure 9b). Thus, dilatant or densifying processes acting on the magma will have a greater marginal influence at low initial porosities than at high initial porosities. In short, our results indicate that an increase or decrease in porosity or permeability will move the magma more-or-less along the paths indicated in panels a and b of Figure 10.

Our results show that permeability can be increased locally by as much as three orders of magnitude due to dilatant processes (see Figure 9, Table 3), even if partial sintering has occurred. Such efficient fluid pathways may play an extremely important role in the outgassing of magmatic volatiles, in turn decreasing the propensity for fluid pressurisation and violent explosive behaviour in active volcanic systems. Fracture geometry (*i.e.* length and aperture) will influence the initial gas volume that can enter and escape through the fracture. If a fracture constitutes a pathway for magmatic fluids to outgas from the system (*e.g.* into the edifice rock: Heiken *et al*., 1988; Kolzenburg *et al*., 2012) then the continuous through-flow of gas has been posited to sustain an open fracture, as long as a there exists a

persistent supply of gas from beneath which is decoupled from the melt (plus crystal) phase of the magma (*e.g.* Rust *et al*., 2004; Plail *et al*., 2014). Indeed, increased pore fluid pressures are thought to occur, albeit transiently, in particle-filled fractures within magma (*e.g.* Castro *et al*., 2014). We anticipate that relatively large volumes of gas can be decoupled from the magma and thus flow through these fractures: a significantly more efficient means of transporting volatiles than bubble migration through a viscous silicate melt, or indeed diffusion-scale processes. We highlight that fractures in magma can allow outgassing even at very low porosities.

As magma fracturing will preferentially occur where strain rates are thought to be highest (*e.g.* Papale, 1999; Gonnerman and Manga, 2003; Edmonds and Herd, 2007), permeable fractures are likely to contribute to a "damage halo" zone surrounding the central conduit (*e.g.* Lavallée *et al.*, 2013; Gaunt *et al.*, 2014; Young and Gottsmann, 2015). Microstructural evidence presented here hints that these fractures occur both in shallow regions (textural evidence of silica polymorphs in fractures point to high-temperature, low-pressure conditions) and deeper in the system (advanced sintering textures observed in some samples indicate high-temperature, high-pressure environments), suggesting that this halo may serve to bleed off volatiles from the magma and promote outgassing into the edifice rock or through near-conduit fracture networks along the length of the conduit. Fault gouge and ash entrained in escaping fluids may accelerate sealing or closure of pathways (*e.g.* Tuffen *et al*., 2003; Saubin *et al*., 2016; Kendrick *et al*., 2016). However, it has been shown experimentally that the relatively slow post-fracture recovery of magma strength may actually promote recrudescent fracture events (Heap *et al*., 2015c), which in turn may serve to regulate lava dome eruptions (Heap *et al*., 2015c; Kendrick *et al*., 2016).

The extraction of magmatic volatiles due to shear strain-induced cavitation—as we observe evidence for herein—has similarly been posited to result in premature embrittlement of magma (Smith *et al*., 2001), assisting the recurrence of fracture events. Repeat faulting events in magma have been proposed as a mechanism for earthquake generation during magma ascent (*e.g.* Tuffen and Dingwell,

2005; Neuberg *et al*., 2006; Lavallée *et al.*, 2008; Tuffen *et al*., 2008; Varley *et al.* 2010a, b; Kendrick *et al.*, 2014a; Heap *et al*., 2015c).

We observe a permeability reduction of an order of magnitude relative to the host material in the sample containing a band of lower porosity characterised by pores that have been variably infilled with ash-sized particles that have sintered to the pore walls. One inference that may be drawn from this is that barriers to flow (viscous densification, sintering of fractures, and infill of pores with granular material or vapour-phase crystallisation) may trap exsolved volatiles and allow the build-up of pore pressure. Iterative densification events may compartmentalise parcels of magma, create pore overpressures, and result in complex permeability anisotropy within the conduit or the dome. We anticipate that the preferential flow of ash-laden fluid along porous networks—that is, interconnected bubble chains or fractures—will cause a time-dependent permeability anisotropy at the periphery of the conduit. The permeability reduction associated with this process (Figure 7, Figure 9a) means that a pathway that preferentially transmits fluids can consequently evolve into a barrier: the relative permeability k_r (Equation 2) will transition from a positive to a negative value). Consequently, fluids will be forced to find another route through the magma.

As previously described, the strain profile across a volcanic conduit or dyke is typically assumed to vary, with strains and strain rates being highest at the margins (*e.g*. Gonnermann and Manga, 2003). Consequently, we may expect fractures in magma to be oriented subparallel to the direction of magma flow (thus in a traditionally-envisaged volcanic conduit, magma fractures will be predominantly oriented subvertically). As such, permeability-increasing fractures will be preferentially oriented in the conduit to facilitate annular or halo outgassing. However, effective sintering of such fractures could promote a build-up of overpressure, by limiting lateral migration of volatiles from the conduit into the edifice or an intermediate fractured zone. There also exists field evidence for the generation of tensile fractures that propagate laterally into the edifice (see Heiken *et al*., 1988; Goto *et al*., 2008). In this case, features acting as pathways for flow will likely improve outgassing into the country rock, whereas barrier-forming features will not majorly influence diffuse edifice outgassing. Similarly,

large-scale fractures throughout a lava dome are often oriented vertically to subvertically (*e.g.* Calder *et al.*, 2015; Walter *et al.*, 2015) and will likely serve to effectively bleed off volatiles. Due to the inherently fractured nature of many lava domes, we anticipate that low-permeability features resulting from local hydrothermal alteration, mineral precipitation, or ash deposition (*e.g.* Edmonds *et al.*, 2003; Ball *et al.*, 2015) may not significantly reduce their overall outgassing potential. However, such sealing of permeable pathways may be of great importance in the shallow conduit, where restricting the migration of an exsolved gas phase could rapidly elevate pore pressure in the system, reducing structural integrity and increasing the likelihood of explosive behaviour.

Furthermore, the length of time that features with high relative permeability can act as effective outgassing networks relies on the interplay between the incumbent stress field, the through-flow of gas (*e.g.* Rust *et al.*, 2004) and effective viscosity- and pressure-dependent densification via compaction or sintering (*e.g.* Quane *et al.*, 2007; Kolzenburg and Russell, 2014; Vasseur *et al.* 2013; Heap *et al.*, 2015c) as well as ancillary processes such as the transport of ash and fault gouge (*e.g.* Tuffen *et al.*, 2003; Kendrick *et al.*, 2015), and hydrothermal mineral precipitation (*e.g.* Edmonds *et al.*, 2003). We emphasise that providing accurate timescales for volcanic processes—even those that are relatively well understood—is inherently problematic due to the lack of knowledge regarding the formation conditions (*e.g.* depth, temperature, local strain rates) or the state of the initial material (porosity, viscosity, grain size distribution etc.). In reality, all of the processes discussed herein are likely to be concurrent within comparable subaerial volcanic systems. The relative proportion of dilatant vs. densifying processes may heavily influence transitions between eruptive regimes and govern, at least partially, repose periods of Vulcanian explosive activity (Quane *et al.*, 2007; Collinson and Neuberg, 2012): dilational processes should bridle eruptive behaviour and lengthen repose times, while sintering and densification should augment the increase of pore pressure, and decrease repose times. Modelling recurrence intervals during periods of intermittent explosive activity is often fraught with complexity (*e.g.* Varley *et al.*, 2006), much of which may be attributed to the contrasting influences of dilatant and densifying processes throughout volcanic systems. However,

this interplay remains poorly understood, and we encourage its description through systematic sets of controlled experiments.

7.2 Considerations for scaling and modelling

The blocks collected for this study were of hand sample size. However, even cursory field observations indicate that variably tabular discontinuities in volcanic material can be seen on much greater lengthscales. Moreover, in the initial stages of their genesis, these features may be orders of magnitude smaller than those discussed herein. Such intra-clast heterogeneity may well be responsible for the large variation in permeabilities measured in volcanic rocks of similar porosities (*e.g.* Mueller *et al.*, 2005; 2008; Farquharson *et al.*, 2015). As the permeability of fractured volcanic rocks is greatly scale-dependent (Heap and Kennedy, 2016), it is of importance that the permeable structures discussed in this contribution are discussed in this context.

Although accurate constraints of subsurface volcanic architecture are rare, results from drilling projects suggest that surficial vent and crater systems on the order of 10s or 100s of m in diameter can belie conduits of relatively narrow width (Mastin and Pollard, 1988). For example, Noguchi *et al.* (2008) describe the dacitic conduit of Mount Unzen (Japan) as ranging from 4 to 40 m in diameter to a depth of 2 km. This is in agreement with studies of exposed feeder dykes (*e.g.* Keating *et al.*, 2008; Galindo and Gudmundsson, 2012), which show that, deeper than around 50 m, solidified dykes tend to have diameters of only a few m. As a consequence, even relatively small discontinuities—such as those described herein—may constitute a non-negligible portion of the conduit width. While the thickness of such features as a proportion of the conduit width will certainly decrease as the conduit widens, we anticipate that in many cases their abundance and longevity will be augmented in shallower systems.

In our study, the equivalent permeability of each block is heavily dependent on its initial size and the area of the discontinuity and the ratios of their permeabilities, just as Equation 1 is strongly influenced

by the ratios of A_s to A_f and k_i to k_f. The partially sintered fracture of COL-V-4, for example, was found to have a permeability of 1.04×10^{-13} m^2, yielding an equivalent permeability of 2.94×10^{-14} m^2 in a core sample of approximately 20 mm diameter (Table 4). To upscale these data, we employ a 1D version of Equation 1, wherein A_s and A_f are substituted for w_s and w_f: the width of the sample and fracture, respectively: $k_f = k_e w_s - k_i(w_s - w_f)/w_f$ (as in Heap and Kennedy, 2016). Hence, a fracture of 2.25 mm width in a sample 10 m wide (with the same host permeability: 1.58×10^{-16} m^2) would result in an equivalent permeability of 1.81×10^{-16} m^2, not significantly higher than that of the host material. In a sample 1000 m in width, the overall influence of the same fracture would be effectively zero ($k_e = 1.58 \times 10^{-16}$ m^2).

In contrast, if the fracture width approaches that of the considered lengthscale, then its influence on equivalent permeability will be correspondingly greater. Similarly, an increase in the number of fractures within a given volume of rock or magma will increase the equivalent permeability to a greater or lesser extent, depending on their geometries and fluid transport properties. These concepts are illustrated in Figure 11, using the example of COL-V-4 (equally, data from other features—Table 4—could be analysed using this method). The lengthscale refers to the total width of material considered, for example the width of a volcanic conduit at a given depth. For reference, the range of widths measured by Noguchi *et al*. (2008) is shaded grey in Figure 11. We highlight that even a single fracture with the thickness and fluid transport properties of that in COL-L-4 can increase the equivalent permeability of a conduit a few m in width (*i.e*. the intersection of the red line with the shaded region). However, the same fracture in a conduit with a diameter of 40 m has a negligible influence. In this simplified context, adding new fractures or widening an existing fracture has the same result, namely increasing the "cumulative fracture width". We highlight that in reality, increasing or decreasing the width of a fracture will introduce complexities associated with non-laminar flow (*e.g*. Heap and Kennedy. 2016), which are not accounted for in Figure 11. Nevertheless, Figure 11 demonstrates the significance of considering upscaling from laboratory samples to outcrop-scale and larger. Accurately incorporating scale effects remains an outstanding challenge in

volcanology, especially in transferring experimental data to eruption models and hazard mitigation policies.

To advance our understanding of volcanic processes and better predict eruptive scenarios requires the development of models which effectively reproduce eruption characteristics observed in nature (*e.g.* Melnik, 2000; Burgisser and Garner, 2005; Collombet, 2009), especially the transitions and timescales between explosive and effusive periods (*e.g.* Jaupart, 1996; Collinson and Neuberg, 2012). Based on our study, we suggest that future models assessing conduit dynamics and permeability evolution consider the propensity for permeability anisotropy within the magma column and lava dome on multiple lengthscales. Given that such heterogeneities are posited to occur primarily at the conduit margins or in high-strain regions of extruding domes, this could be modelled by stochastic inclusion of transient variations in magma permeability, by a coupling of permeability and shear strain across the width of the conduit, or by the calculation of the (time-dependent) equivalent permeability of fracturing conduit margins (as touched on in Figure 11 and the attendant discussion).

7.3 Field interpretations

We note that in the absence of microstructural examination, interpretation of some textural or structural heterogeneities encountered in volcanic materials can be nontrivial. Despite being visually similar at a hand sample scale, our study has shown that these features are not equally efficient at transmitting fluids. Thus we highly recommend that any interpretation of heterogeneity-bearing volcanic rocks—especially with respect to their influence on permeability and the attendant implications for outgassing—should be buttressed by microstructural description and/or measurements of permeability or porosity.

As a final comment: due to the accretionary growth of stratovolcanoes (*e.g.* Odbert *et al.*, 2015), explosively or effusively erupted lava eventually comprises some portion of the edifice. Thus, if fluid flow pathways or barriers are erupted and preserved—as was the case with our sample set—we may

also expect them to increase permeability anisotropy and influence fluid partitioning within the edifice. We anticipate their presence throughout the upper edifice at Volcán de Colima and indeed at other comparable volcanic systems (such discontinuity-bearing rocks can be seen at throughout the Taupō Volcanic Zone in New Zealand for example). However, a quantitative analysis of their appearance at the surface could be somewhat misleading. For example, it has been noted that features that provide effective outgassing pathways are, by definition, less likely to be erupted out of the volcano than ineffective (or nonexistant) pathways (Plail *et al*., 2014). Similarly, Castro *et al*. (2012) intimates that the pyroclastic origin of tuffisite-bearing bombs indicates that systems containing highly permeable discontinuities can still be subject to significant overpressure development. Further, the preservation of clasts containing fractures may be poor, especially if the fracture is poorly-sintered. Nevertheless, we stress that discontinuity-bearing volcanic materials can provide incredibly informative snapshots of otherwise unobservable magmatic processes, making their continued study a valuable pursuit in volcanology.

8. Concluding remarks

Tabular heterogeneities in andesitic rocks—of both explosive and effusive origin—can be found in abundance at Volcán de Colima (Mexico), providing frozen-in snapshots of magmatic processes. Alongside an examination of their microstructure, a systematic laboratory study of the physical properties of a selection of these heterogeneity-bearing blocks allows us to glean important information regarding the likely geneses of these features within a volcanic system, as well as their influence on the physical properties of the magma (at least upon eruption). Bands were inferred to form in high-porosity pumice blocks (ϕ around 0.30 and higher) due to inhomogeneous bubble expansion in magma. Despite a significant influence on the porosity of these samples, permeabilities of banded and non-banded pumice were found to be comparable (of the order 10^{-13} m^2). This is thought to be due to the pre-established pathways of effectively connected porosity. In lower porosity blocks ($\phi < 0.20$), features are preserved that increase porosity and permeability relative to the

surrounding material. We suggest that these discontinuities may be the frozen relicts of dilatant processes such as viscous cavitation or magma fracturing. We find that these fractures can increase in permeability by about three orders of magnitude relative to the host rock, when they are oriented parallel to fluid flow. Evidence of subsequent fracture healing can also be observed in our microstructure, and our measurements indicate that fracture permeability decreases with more advanced sintering. Differences in the extent of sintering, and the presence of silica polymorphs in some samples, suggest that these features were likely formed at different depths in the conduit. The evidence therefore suggests that fractures exist—although in some cases, only temporarily—along an extensive portion of the conduit, supporting the concept of a permeable outgassing halo surrounding the conduit. Notably, textures interpreted herein as the infill of pores with transiently granular material (such as gas-transported volcanic ash) indicates that porous networks may subsequently become barriers to fluid flow over time, especially when oriented normal to fluid flow. This highlights a complex interplay between dilatant and densifying processes in magma, as well as the time-dependent evolution of its physical properties. We have presented evidence for significant permeability variation within conduit magma and dome at Volcán de Colima, and we anticipate that the features described here will also exist at similar andesitic stratovolcanoes worldwide, at a range of lengthscales. We contest that localised permeability heterogeneities must be a critical parameter influencing the evolution of pressures within active volcanic systems, and use a simple upscaling model to illustrate the evolving significance of permeability heterogeneities over different lengthscales. It is likely that, in turn, these features will likely influence the eruptive regime and recurrence intervals of explosions or degassing events at active volcanoes.

Acknowledgements

Oliver Lamb, Tom McLaughlin, Graeme Alexander William Sinclair, and Josh Greenwood are thanked for their assistance during the field campaign. Fieldwork was funded in part by the

framework of the LABEX ANR-11-LABX-0050_G-EAU-THERMIE-PROFONDE and therefore benefits from a funding from the state managed by the French National Research Agency as part of the Investments for the future program. JIF acknowledges an Initiative d'Excellence (IDEX) "Contrats doctoraux" grant from the French State. MJH acknowledges Initiative d'Excellence (IDEX) Attractivité grant "VOLPERM". YL acknowledges a Natural Environment Research Council grant (NE/M013561/1) as well as the European Research Council for a Starting Grant on Strain Localisation in Magmas (SLiM, No 306488). NV thanks the Universidad de Colima for its assistance via FRABA 2014. Gilles Morvan is thanked for his assistance on the SEM. We are also thankful to Jackie Kendrick, Alexandra Kushnir, Kelly Russell, Stephan Kolzenburg, and Fabian Wadsworth for helpful discussions of the microstructure. We also thank Katherine Cashman and an anonymous reviewer for their constructive reviews.

References

Andrews, G.D.M., Russell, J.K., Stewart, M.I. (2014). The history and dynamics of a welded pyroclastic dam and its failure. Bull. Volcanol. 76, 811.

Bagdassarov, N. S., and Dingwell, D. B. (1992). A rheological investigation of vesicular rhyolite. Journal of Volcanology and Geothermal Research, 50(3), 307-322.

Ball, J.L., Stauffer, P.H., Calder, E.S. and Valentine, G.A., (2015). The hydrothermal alteration of cooling lava domes. Bull. of Volcanol., 77(12), pp.1-16.

Baud, P., Meredith, P., and Townend, E. (2012). Permeability evolution during triaxial compaction of an anisotropic porous sandstone. Journal of Geophysical Research: Solid Earth (1978–2012), 117(B5).

Bense, V. F., and Person, M. A. (2006). Faults as conduit-barrier systems to fluid flow in siliciclastic sedimentary aquifers. Water Resources Research, 42(5).

Berlo, K., Tuffen, H., Smith, V. C., Castro, J. M., Pyle, D. M., Mather, T. A., and Geraki, K. (2013). Element variations in rhyolitic magma resulting from gas transport. Geochimica et Cosmochimica Acta, 121, 436-451.

Branney, M.J., Kokelaar, B.P., McConnell, B.J. (1992). The Bad Step Tuff: a lava-like rheomorphic ignimbrite in a calc-alkaline piecemeal caldera, English Lake District. Bull. Volcanol. 54, 187–199.

Bruhn, R. L., Yonkee, W. A., and Parry, W. T. (1990). Structural and fluid-chemical properties of seismogenic normal faults. Tectonophysics, 175(1), 139-157.

Buisson C and Merle O (2002) Experiments on internal strain in lava dome cross sections. Bull. Volcanol., 64(6), pp.363-371.

Burgisser, A., Arbaret, L., Druitt, T. H., and Giachetti, T. (2011). Pre-explosive conduit conditions of the 1997 Vulcanian explosions at Soufriere Hills Volcano, Montserrat: II. Overpressure and depth distributions. Journal of Volcanology and Geothermal Research, 199(3), 193-205.

Burgisser, A., Poussineau, S., Arbaret, L., Druitt, T. H., Giachetti, T., and Bourdier, J. L. (2010). Pre-explosive conduit conditions of the 1997 Vulcanian explosions at Soufrière Hills Volcano, Montserrat: I. Pressure and vesicularity distributions. Journal of Volcanology and Geothermal Research, 194(1), 27-41.

Burgisser, A., and Gardner, J. E. (2004). Experimental constraints on degassing and permeability in volcanic conduit flow. Bull. Volcanol., 67(1), 42-56.

Cabrera, A., Weinberg, R. F., and Wright, H. M. (2015). Magma Fracturing and Degassing Associated with Obsidian Formation: The Explosive-Effusive Transition. Journal of Volcanology and Geothermal Research.

Cagnoli, B., Barmin, A., Melnik, O., and Sparks, R. S. J. (2002). Depressurization of fine powders in a shock tube and dynamics of fragmented magma in volcanic conduits. Earth and Planetary Science Letters, 204(1), 101-113.

Caine, J. S., Evans, J. P., and Forster, C. B. (1996). Fault zone architecture and permeability structure. Geology, 24(11), 1025-1028.

Capra, L., Macías, J.L., Cortés, A., Dávila, N., Saucedo, R., Osorio-Ocampo, S., Arce, J.L., Gavilanes-Ruíz, J.C., Corona-Chávez, P., García-Sánchez, L. and Sosa-Ceballos, G., (2015).

Preliminary report on the July 10–11, 2015 explosive eruption at Volcán de Colima: Pyroclastic density currents with exceptional runouts and volume. Journal of Volcanology and Geothermal Research.

Caricchi, L., Burlini, L., Ulmer, P., Gerya, T., Vassalli, M., and Papale, P. (2007). Non-Newtonian rheology of crystal-bearing magmas and implications for magma ascent dynamics. Earth and Planetary Science Letters, 264(3), 402-419.

Cashman, K. V. (1992). Groundmass crystallization of Mount St. Helens dacite, 1980–1986: a tool for interpreting shallow magmatic processes. Contributions to Mineralogy and Petrology, 109(4), 431-449.

Cashman, S. M., and Cashman, K. V. (2006). Cataclastic textures in La Grange fault rocks, Klamath Mountains, California. Geological Society of America Special Papers, 410, 433-450.

Cashman, K. V., Thornber, C. R., and Pallister, J. S. (2008). From dome to dust: Shallow crystallization and fragmentation of conduit magma during the 2004-2006 dome extrusion of Mount St. Helens, Washington. US Geological Survey professional paper, (1750), 387-413.

Castro, J. M., Manga, M., and Martin, M. C. (2005). Vesiculation rates of obsidian domes inferred from H_2O concentration profiles. Geophysical Research Letters, 32(21).

Castro, J. M., Bindeman, I. N., Tuffen, H., and Schipper, C. I. (2014). Explosive origin of silicic lava: Textural and δD–H 2 O evidence for pyroclastic degassing during rhyolite effusion. Earth and Planetary Science Letters, 405, 52-61.

Castro, J. M., Cordonnier, B., Tuffen, H., Tobin, M. J., Puskar, L., Martin, M. C., and Bechtel, H. A. (2012). The role of melt-fracture degassing in defusing explosive rhyolite eruptions at volcán Chaitén. Earth and Planetary Science Letters, 333, 63-69.

Chester, F. M., and Logan, J. M. (1986). Implications for mechanical properties of brittle faults from observations of the Punchbowl fault zone, California. Pure and Applied Geophysics, 124(1-2), 79-106.

Chevrel, M. O., Cimarelli, C., deBiasi, L., Hanson, J. B., Lavallée, Y., Arzilli, F., and Dingwell, D. B. (2015). Viscosity measurements of crystallizing andesite from Tungurahua volcano (Ecuador). Geochemistry, Geophysics, Geosystems, 16(3), 870-889.

Chevrel, M. O., Platz, T., Hauber, E., Baratoux, D., Lavallée, Y., and Dingwell, D. B. (2013). Lava flow rheology: A comparison of morphological and petrological methods. Earth and Planetary Science Letters, 384, 109-120.

Chokshi, A. H. (1997). A comparative examination of superplastic flow and fracture in metals and ceramics. Materials Science and Engineering: A, 234, 986-990.

Collombet, M. (2009). Two-dimensional gas loss for silicic magma flows: toward more realistic numerical models. Geophysical Journal International, 177(1), 309-318.

Cordonnier, B., Caricchi, L., Pistone, M., Castro, J., Hess, K. U., Gottschaller, S., Manga, M., Dingwell, D. B., and Burlini, L. (2012). The viscous-brittle transition of crystal-bearing silicic melt: Direct observation of magma rupture and healing. Geology, 40(7), 611-614.

Costa, A., and Macedonio, G. (2003). Viscous heating in fluids with temperature-dependent viscosity: implications for magma flows. Nonlinear Processes in Geophysics, 101 - 111.

Damby, D. E., Llewellin, E. W., Horwell, C. J., Williamson, B. J., Najorka, J., Cressey, G., and Carpenter, M. (2014). The-phase transition in volcanic cristobalite. Journal of Applied Crystallography, 47(4).

De Maisonneuve, C. B., Bachmann, O., and Burgisser, A. (2009). Characterization of juvenile pyroclasts from the Kos Plateau Tuff (Aegean Arc): insights into the eruptive dynamics of a large rhyolitic eruption. Bull. Volcanol., 71(6), 643-658.

De Vries, B. V. W., and Borgia, A. (1996). The role of basement in volcano deformation. Geological Society, London, Special Publications, 110(1), 95-110.

De Vries, B. V. W., and Merle, O. (1998). Extension induced by volcanic loading in regional strike-slip zones. Geology, 26(11), 983-986.

Deer, W. A., Howie, R. A., and Zussman, J. (1996). An introduction to the rock forming minerals. Longman Scientific and Technical, New York.

Deng, S., L. Zuo, A. Aydin, J. Dvorkin, and T. Mukerji (2015), Permeability characterization of natural compaction bands using core flooding experiments and three-dimensional image-based analysis: Comparing and contrasting the results from two different methods, AAPG Bull., 99, 27–49.

Denlinger, R. P., and Hoblitt, R. P. (1999). Cyclic eruptive behavior of silicic volcanoes. Geology, 27(5), 459-462.

Dingwell, D.B., 1996, Volcanic dilemma: Flow or blow?: Science, v. 273, p. 1054–1055.

Dingwell D.B., Lavallée Y., Hess K.-U., Flaws A., Marti J., Nichols A.R.L., Gilg H.A., Schillinger B., 2015. Eruptive shearing in tube pumice: pure and simple. Solid Earth Discussion. 7, 3053-3085.

Edmonds, M., and Herd, R. A. (2007). A volcanic degassing event at the explosive-effusive transition. Geophysical Research Letters, 34(21).

Edmonds, M., Oppenheimer, C., Pyle, D.M., Herd, R.A. and Thompson, G., (2003) SO_2 emissions from Soufrière Hills Volcano and their relationship to conduit permeability, hydrothermal interaction and degassing regime. Journal of Volcanology and Geothermal Research, 124(1), 23-43.

Eichelberger, J. C., Carrigan, C. R., Westrich, H. R., and Price, R. H. (1986). Non-explosive silicic volcanism. Nature, 323(6089), 598-602.

Farquharson, J. I., Heap, M. J., Varley, N. R., Baud, P., and Reuschlé, T. (2015). Permeability and porosity relationships of edifice-forming andesites: A combined field and laboratory study. Journal of Volcanology and Geothermal Research, 297, 52-68.

Fink, J. H., and Kieffer, S. W. (1993). Estimate of pyroclastic flow velocities resulting from explosive decompression of lava domes. Nature, 363(6430), 612-615.

Fink, J. H., and Manley, C. R. (1987). Origin of pumiceous and glassy textures in rhyolite flows and domes. Geological Society of America Special Papers, 212, 77-88.

Forchheimer, P. (1901). Wasserbewegung durch boden. Z. Ver. Deutsch. Ing,45(1782), 1788.

Galindo, I., and Gudmundsson, A. (2012). Basaltic feeder dykes in rift zones: geometry, emplacement, and effusion rates. Natural Hazards and Earth System Sciences, 12(12), 3683-3700.

Gaunt, H. E., Sammonds, P. R., Meredith, P. G., Smith, R., and Pallister, J. S. (2014). Pathways for degassing during the lava dome eruption of Mount St. Helens 2004–2008. Geology, 42(11), 947-950.

Gerst, A., and Savage, M. K. (2004). Seismic anisotropy beneath Ruapehu volcano: A possible eruption forecasting tool. Science, 306(5701), 1543-1547.

Giordano, D., Russell, J. K., and Dingwell, D. B. (2008). Viscosity of magmatic liquids: a model. Earth and Planetary Science Letters, 271(1), 123-134.

Gonnermann, H. M., and Manga, M. (2005). Flow banding in obsidian: A record of evolving textural heterogeneity during magma deformation. Earth and Planetary Science Letters, 236(1), 135-147.

Gonnermann, H. M., and Manga, M. (2003). Explosive volcanism may not be an inevitable consequence of magma fragmentation. Nature, 426(6965), 432-435.

Goto, A. (1999). A new model for volcanic earthquake at Unzen Volcano: melt rupture model. Geophysical Research Letters, 26(16), 2541-2544.

Goto, Y., Nakada, S., Kurokawa, M., Shimano, T., Sugimoto, T., Sakuma, S., Hoshizumi, H., Yoshimoto, M. and Uto, K., (2008) Character and origin of lithofacies in the conduit of Unzen volcano, Japan. Journal of Volcanology and Geothermal Research, 175(1), pp.45-59.

Griffiths, R. W., and Fink, J. H. (1993). Effects of surface cooling on the spreading of lava flows and domes. Journal of Fluid Mechanics, 252, 667-702.

Gruzdkov, A. A., and Petrov, Y. V. (2008). Cavitation breakup of low-and high-viscosity liquids. Technical Physics, 53(3), 291-295.

Hale, A. J., and Mülhaus, H. B. (2007). Modelling shear bands in a volcanic conduit: Implications for over-pressures and extrusion-rates. Earth and Planetary Science Letters, 263(1), 74-87.

Hall, M. L., Robin, C., Beate, B., Mothes, P., and Monzier, M. (1999). Tungurahua Volcano, Ecuador: structure, eruptive history and hazards. Journal of Volcanology and Geothermal Research, 91(1), 1-21.

Heap, M. J., Farquharson, J. I., Wadsworth, F. B., Kolzenburg, S., and Russell, J. K. (2015c). Timescales for permeability reduction and strength recovery in densifying magma. Earth and Planetary Science Letters, 429, 223-233.

Heap, M. J., Baud, P., Reuschlé, T., and Meredith, P. G. (2014c). Stylolites in limestones: Barriers to fluid flow? Geology, 42(1), 51-54.

Heap, M. J., Farquharson, J. I., Baud, P., Lavallée, Y., and Reuschlé, T. (2015a). Fracture and compaction of andesite in a volcanic edifice. Bull. Volcanol.

Heap, M. J., Kolzenburg, S., Russell, J. K., Campbell, M. E., Welles, J., Farquharson, J. I., and Ryan, A. (2014a). Conditions and timescales for welding block-and-ash flow deposits. Journal of Volcanology and Geothermal Research, 289, 202-209.

Heap, M. J., Lavallée, Y., Petrakova, L., Baud, P., Reuschle, T., Varley, N. R., and Dingwell, D. B. (2014b). Microstructural controls on the physical and mechanical properties of edifice-forming andesites at Volcán de Colima, Mexico. Journal of Geophysical Research: Solid Earth, 119(4), 2925-2963.

Heap, M. J., Xu, T., Kushnir, A. R. L., Kennedy, B. M., and Chen, C. F. (2015b). Fracture of magma containing overpressurised pores. Journal of Volcanology and Geothermal Research.

Heap, M. J. and Kennedy, B. (2016). Exploring the scale-dependent permeability of fractured andesite. In review.

Heiken, G., Wohletz, K., and Eichelberger, J. (1988). Fracture fillings and intrusive pyroclasts, Inyo Domes, California. Journal of Geophysical Research: Solid Earth, 93(B5), 4335-4350.

Hornby AJ, Kendrick JE, Lamb OD, Hirose T, De Angelis S, Aulock FW, Umakoshi K, Miwa T, Henton De Angelis S, Wadsworth FB, Hess KU (2015) Spine growth and seismogenic faulting at Mt. Unzen, Japan. Journal of Geophysical Research: Solid Earth. Jun 1;120(6):4034-54.

James, M. R., and Varley, N. R. (2012). Identification of structural controls in an active lava dome with high resolution DEMs: Volcán de Colima, Mexico. Geophysical Research Letters, 39(22).

Jaupart, C., and Allègre, C. J. (1991). Gas content, eruption rate and instabilities of eruption regime in silicic volcanoes. Earth and Planetary Science Letters,102(3), 413-429.

Keating, G. N., Valentine, G. A., Krier, D. J., and Perry, F. V. (2008). Shallow plumbing systems for small-volume basaltic volcanoes. Bull. Volcanol., 70(5), 563-582.

Kendrick J. E., Lavallée Y, Varley N. R., Wadsworth F. B., Vasseur J., and Lamb, O. (2016). Blowing off steam: Sintering fragmented pyroclastic material to form tuffisites. Frontiers in Earth Science, Submitted.

Kendrick, J. E., Lavallée, Y., Ferk, A., Perugini, D., Leonhardt, R., and Dingwell, D. B. (2012). Extreme frictional processes in the volcanic conduit of Mount St. Helens (USA) during the 2004–2008 eruption. Journal of Structural Geology, 38, 61-76.

Kendrick, J. E., Lavallée, Y., Hess, K. U., Heap, M. J., Gaunt, H. E., Meredith, P. G., and Dingwell, D. B. (2013). Tracking the permeable porous network during strain-dependent magmatic flow. Journal of Volcanology and Geothermal Research, 260, 117-126.

Kendrick, J. E., Lavallée, Y., Hirose, T., Di Toro, G., Hornby, A. J., De Angelis, S., and Dingwell, D. B. (2014a). Volcanic drumbeat seismicity caused by stick-slip motion and magmatic frictional melting. Nature Geoscience, 7(6), 438-442.

Kendrick, J. E., Lavallée, Y., Hess, K. U., De Angelis, S., Ferk, A., Gaunt, H. E., Meredith, P. G., Dingwell, D. B. and Leonhardt, R. (2014b). Seismogenic frictional melting in the magmatic column. Solid Earth, 5(1), 199-208.

Kennedy, B. M., Spieler, O., Scheu, B., Kueppers, U., Taddeucci, J., and Dingwell, D. B. (2005). Conduit implosion during Vulcanian eruptions. Geology, 33(7), 581-584.

Kennedy, B. M., Wadsworth, F. B., Schipper, C. I., Jellinek, M., Vasseur, J., von Aulock, F. W., Hess, K.-U., Russell, K., Lavallée, Y., Nichols, A. R. L., and Dingwell, D. B. (2015). Surface tension densifies magma but maintains permeability. Earth and Planetary Science Letters 433, 116-124.

Klinkenberg, L. J. (1941). The permeability of porous media to liquids and gases. In Drilling and production practice. American Petroleum Institute.

Kolzenburg, S., and Russell, J. K. (2014). Welding of pyroclastic conduit infill: A mechanism for cyclical explosive eruptions. Journal of Geophysical Research: Solid Earth, 119(7), 5305-5323.

Kolzenburg, S., Heap, M. J., Lavallée, Y., Russell, J. K., Meredith, P. G., and Dingwell, D. B. (2012). Strength and permeability recovery of tuffisite-bearing andesite. Solid Earth, 3(2), 191-198.

Koyaguchi, T., Scheu, B., Mitani, N. K., and Melnik, O. (2008). A fragmentation criterion for highly viscous bubbly magmas estimated from shock tube experiments. Journal of Volcanology and Geothermal Research, 178(1), 58-71.

Kueppers, U., Scheu, B., Spieler, O., and Dingwell, D. B. (2005). Field-based density measurements as tool to identify preeruption dome structure: set-up and first results from Unzen volcano, Japan. Journal of Volcanology and Geothermal Research, 141(1), 65-75.

Kushnir, A.R.L., Martel, C., Bourdier, J.-L., Heap, M.J., Reuschlé, T., Erdmann, S., Komorowski, C., Cholik, N. (2016). Probing permeability and microstructure: Unravelling the role of a low-permeability dome on the explosivity of Merapi (Indonesia). Journal of Volcanology and Geothermal Research. 316, 56-71. doi:10.1016/j.jvolgeores.2016.02.012.

La Coordinación Nacional de Protección Civil (2015a). Reporte de situación actual del Volcán de Colima [Report of the current state of Volcán de Colima]. Mexico City, México, D.F., 11 July 2015. (In Spanish) [Available at:
http://portal.proteccioncivil.gob.mx/sala_prensa/archivos/Files/np_4102.pdf]

La Coordinación Nacional de Protección Civil (2015b). Reporte de situación actual del Volcán de Colima [Report of the current state of Volcán de Colima]. Mexico City, México, D.F., 13 July 2015. (In Spanish) [Available at:
http://portal.proteccioncivil.gob.mx/sala_prensa/archivos/Files/np_416_13_JULIO_actividad_volcan_de_colima2.pdf]

Laumonier, M., Arbaret, L., Burgisser, A., and Champallier, R. (2011). Porosity redistribution enhanced by strain localization in crystal-rich magmas. Geology, 39(8), 715-718.

Lavallée Y., Wadsworth F.B., Vasseur J., Russell J.K., Andrews G.D.M., Hess K.-U., Aulock F., Kendrick J.E., Tuffen H., Biggin A.J., Dingwell D.B., 2015. Eruption and emplacement timescales of ignimbrite super-eruptions from thermo-kinetics of glass shards. Frontiers in Earth Sciences 3:2. doi: 10.3389/feart.2015.00002.

Lavallée, Y., Benson, P. M., Heap, M. J., Hess, K. U., Flaws, A., Schillinger, B., and Dingwell, D. B. (2013). Reconstructing magma failure and the degassing network of dome-building eruptions. Geology, 41(4), 515-518.

Lavallée, Y., Heap, M.J., Kueppers, U., Kendrick, J. and Dingwell, D.B. (2016) The Fragility of Volcán de Colima- a material constraint. In: Varley, N. and Komorowski, J-C., eds Volcán de Colima: Managing the threat. Active Volcanoes of the World. Springer, New York. ISBN 978-3-642-25910-4 (In Press)

Lavallée, Y., Hess, K. U., Cordonnier, B., and Dingwell, D. B. (2007). Non-Newtonian rheological law for highly crystalline dome lavas. Geology, 35(9), 843-846.

Lavallée, Y., Meredith, P. G., Dingwell, D. B., Hess, K. U., Wassermann, J., Cordonnier, B., and Kruhl, J. H. (2008). Seismogenic lavas and explosive eruption forecasting. Nature, 453(7194), 507-510.

Lavallée, Y., Varley, N. R., Alatorre-Ibargüengoitia, M. A., Hess, K. U., Kueppers, U., Mueller, S., ... and Dingwell, D. B. (2012). Magmatic architecture of dome-building eruptions at Volcán de Colima, Mexico. Bulletin of volcanology, 74(1), 249-260.

Luhr, J.F., 2002. Petrology and geochemistry of the 1991 and 1998-1999 lava flows from Volcán de Colima, Mexico: implications for the end of the current eruptive cycle. Journal of Volcanology and Geothermal Research, 117(1-2): 169-194.

Mackenzie, J., and R. Shuttleworth (1949), A phenomenological theory of sintering, Proc. Phys. Soc. Sect. B,62(12), 833.

Martel C, Dingwell DB, Spieler O, Pichavant M, Wilke M (2000) Fragmentation of foamed silicic melts: an experimental study. Earth Plan. Sci. Lett. 178, 47 - 58.

Massol, H., and Jaupart, C. (2009). Dynamics of magma flow near the vent: Implications for dome eruptions. Earth and Planetary Science Letters, 279(3), 185-196.

Mastin, L. G. (2002). Insights into volcanic conduit flow from an open-source numerical model. Geochemistry, Geophysics, Geosystems, 3(7), 1-18.

Mastin, L. G., and Pollard, D. D. (1988). Surface deformation and shallow dike intrusion processes at Inyo Craters, Long Valley, California. Journal of Geophysical Research: Solid Earth, 93(B11), 13221-13235.

Mellors, R.A., Sparks, R.S.J. (1991). Spatter-rich pyroclastic flow deposits on Santorini, Greece. Bull. Volcanol. 53, 327–342.

Melnik, O. (2000). Dynamics of two-phase conduit flow of high-viscosity gas-saturated magma: large variations of sustained explosive eruption intensity. Bull. Volcanol., 62(3), 153-170.

Michaut, C., Ricard, Y., Bercovici, D., and Sparks, R. S. J. (2013). Eruption cyclicity at silicic volcanoes potentially caused by magmatic gas waves. Nature Geoscience, 6(10), 856-860.

Michol, K.A., Russell, J.K. and Andrews, G.D.M. (2008). Welded block and ash flow deposits from Mount Meager, British Columbia, Canada. Journal of Volcanology and Geothermal Research, 169(3), 121-144.

Mueller S., Melnik O., Spieler O., Scheu B., Dingwell D.B. (2005), Permeability and degassing of dome lavas undergoing rapid decompression: An experimental determination: Bulletin of Volcanology, 67, p. 526– 538, doi: 10.1007/s00445-004-0392-4.

Mueller, S., Scheu, B., Kueppers, U., Spieler, O., Richard, D., and Dingwell, D. B. (2011). The porosity of pyroclasts as an indicator of volcanic explosivity. Journal of Volcanology and Geothermal Research, 203(3), 168-174.

Mueller, S., Scheu, B., Spieler, O., and Dingwell, D. B. (2008). Permeability control on magma fragmentation. Geology, 36(5), 399-402.

Mueller, S.P., (2006). Permeability and porosity as constraints on the explosive eruption of magma: laboratory experiments and field investigations. (PhD Thesis). University of Munich, Munich, Germany.

Namiki, A., and Manga, M. (2005). Response of a bubble bearing viscoelastic fluid to rapid decompression: implications for explosive volcanic eruptions. Earth and Planetary Science Letters, 236(1), 269-284.

Navon, O., Chekhmir, A., and Lyakhovsky, V. (1998). Bubble growth in highly viscous melts: theory, experiments, and autoexplosivity of dome lavas. Earth and Planetary Science Letters, 160(3), 763-776.

Neuberg, J. W., Tuffen, H., Collier, L., Green, D., Powell, T., and Dingwell, D. (2006). The trigger mechanism of low-frequency earthquakes on Montserrat. Journal of Volcanology and Geothermal Research, 153(1), 37-50.

Nguyen, C. T., Gonnermann, H. M., and Houghton, B. F. (2014). Explosive to effusive transition during the largest volcanic eruption of the 20th century (Novarupta 1912, Alaska). Geology, 42(8), 703-706.

Noguchi, S., Toramaru, A. and Nakada, S. (2008) Groundmass crystallization in dacite dykes taken in Unzen scientific drilling project (USDP-4). J. Volcanol. Geotherm. Res. 175, 71–81.

Odbert, H., Taisne, B., and Gottsmann, J. (2015). Deposit loading and its effect on co-eruptive volcano deformation. Earth and Planetary Science Letters, 413, 186-196.

Okumura, S., and Sasaki, O. (2014). Permeability reduction of fractured rhyolite in volcanic conduits and its control on eruption cyclicity. Geology, 42(10), 843-846.

Okumura, S., Nakamura, M., Takeuchi, S., Tsuchiyama, A., Nakano, T., and Uesugi, K. (2009). Magma deformation may induce non-explosive volcanism via degassing through bubble networks. Earth and Planetary Science Letters, 281(3), 267-274.

Okumura, S., Nakamura, M., Uesugi, K., Nakano, T., and Fujioka, T. (2013). Coupled effect of magma degassing and rheology on silicic volcanism. Earth and Planetary Science Letters, 362, 163-170.

Pallister, J. S., Cashman, K. V., Hagstrum, J. T., Beeler, N. M., Moran, S. C., and Denlinger, R. P. (2013). Faulting within the Mount St. Helens conduit and implications for volcanic earthquakes. Geological Society of America Bulletin, 125(3-4), 359-376.

Papale, P. (1999). Strain-induced magma fragmentation in explosive eruptions. Nature, 397(6718), 425-428.

Plail, M., Edmonds, M., Humphreys, M. C., Barclay, J., and Herd, R. A. (2014). Geochemical evidence for relict degassing pathways preserved in andesite. Earth and Planetary Science Letters, 386, 21-33.

Renard, P., and De Marsily, G. (1997). Calculating equivalent permeability: a review. Advances in Water Resources, 20(5), 253-278.

Richard, D., Scheu, B., Mueller, S.P., Spieler, O., Dingwell, D.B., 2013. Outgassing: influence on speed of magma fragmentation. J. Geophys. Res. Solid Earth 118, 862–877. http:// dx.doi.org/10.1002/jgrb.50080

Roman, D. C., Moran, S. C., Power, J. A., and Cashman, K. V. (2004). Temporal and spatial variation of local stress fields before and after the 1992 eruptions of Crater Peak vent, Mount Spurr volcano, Alaska. Bulletin of the Seismological Society of America, 94(6), 2366-2379.

Rust, A. C., Cashman, K. V., and Wallace, P. J. (2004). Magma degassing buffered by vapor flow through brecciated conduit margins. Geology, 32(4), 349-352.

Sánchez, M. C., Sarrionandia, F., Arostegui, J., Eguiluz, L., & Ibarguchi, J. G. (2012). The transition of spatter to lava-like body in lava fountain deposits: features and examples from the Cabezo Segura volcano (Calatrava, Spain). Journal of Volcanology and Geothermal Research, 227, 1-14.

Saubin, E., Tuffen, H., Gurioli, L., Owen, J., Castro, J. M., Berlo, K., McGowan, E., Schipper, C. I. and Wehbe, K. (2016) Conduit dynamics in transitional rhyolitic activity recorded by tuffisite vein textures from the 2008-2009 Chaitén eruption. Frontiers in Earth Science, *in press*.

Schaefer, L. N., Kendrick, J. E., Lavallée, Y., Oommen, T., and Chigna, G. (2015). Geomechanical rock properties of a basaltic volcano. Frontiers in Earth Science, 3, 29.

Schneider, C. A.; Rasband, W. S. and Eliceiri, K. W. (2012), "NIH Image to ImageJ: 25 years of image analysis", Nature methods 9(7): 671-675, PMID 22930834.

Schultz, R. A., and Fossen, H. (2008). Terminology for structural discontinuities. AAPG bulletin, 92(7), 853-867.

Smith, J. V., Miyake, Y., and Oikawa, T. (2001). Interpretation of porosity in dacite lava domes as ductile–brittle failure textures. Journal of Volcanology and Geothermal Research, 112(1), 25-35.

Song, W., Hess, K. U., Damby, D. E., Wadsworth, F. B., Lavallée, Y., Cimarelli, C., & Dingwell, D. B. (2014). Fusion characteristics of volcanic ash relevant to aviation hazards. Geophysical Research Letters, 41(7), 2326-2333.

Sousa, L. L., Souza, A. D., Fernandes, L., Arantes, V. L., and Salomão, R. (2015). Development of densification-resistant castable porous structures from in situ mullite. Ceramics International.

Sparks, R.S.J., (1997), Causes and consequences of pressurisation in lava dome eruptions: Earth and Planetary Science Letters. 150, 177-189.

Sparks, R. S. J., S. R. Tait, and Y. Yanev (1999), Dense welding caused by volatile resorption, J. Geol. Soc., 156, 217–225, doi:10.1144/gsjgs.156.2.0217.

Spieler, O., Kennedy, B., Kueppers, U., Dingwell, D. B., Scheu, B., and Taddeucci, J. (2004). The fragmentation threshold of pyroclastic rocks. Earth and Planetary Science Letters, 226(1), 139-148.

Stasiuk, M. V., Barclay, J., Carroll, M. R., Jaupart, C., Ratté, J. C., Sparks, R. S. J., and Tait, S. R. (1996). Degassing during magma ascent in the Mule Creek vent (USA). Bull. Volcanol., 58(2-3), 117-130.

Streck, M. J., and Grunder, A. L. (1995). Crystallization and welding variations in a widespread ignimbrite sheet; the Rattlesnake Tuff, eastern Oregon, USA. Bull. Volcanol., 57(3), 151-169.

Tuffen, H., and Dingwell, D. (2005). Fault textures in volcanic conduits: evidence for seismic trigger mechanisms during silicic eruptions. Bull. Volcanol.,67(4), 370-387.

Tuffen, H., Dingwell, D. B., and Pinkerton, H. (2003). Repeated fracture and healing of silicic magma generate flow banding and earthquakes?. Geology,31(12), 1089-1092.

Tuffen, H., Smith, R., and Sammonds, P. R. (2008). Evidence for seismogenic fracture of silicic magma. Nature, 453(7194), 511-514.

Varley, N. R., Arámbula-Mendoza, R., Reyes-Dávila, G., Stevenson, J., and Harwood, R. (2010a). Long-period seismicity during magma movement at Volcán de Colima. Bull. Volcanol., 72(9), 1093-1107.

Varley, N. R., Arámbula-Mendoza, R., Reyes-Dávila, G., Sanderson, R., and Stevenson, J. (2010b). Generation of Vulcanian activity and long-period seismicity at Volcán de Colima, Mexico. Journal of Volcanology and Geothermal Research, 198(1), 45-56.

Varley, N. R., Johnson, J., Ruiz, M., Reyes-Dávila, G. A. and Martin, K., 2006. Applying statistical analysis to understanding the dynamics of volcanic explosions. In: H.M. Mader, S.G. Coles, C.B. Connor and L.J. Connor (Editors), Statistics in Volcanology. Special publication of IAVCEI, pp. 57-76.

Vasseur, J., Wadsworth, F. B., Lavallée, Y., Hess, K. U., and Dingwell, D. B. (2013). Volcanic sintering: Timescales of viscous densification and strength recovery. Geophysical Research Letters, 40(21), 5658-5664.

Venezky, D. Y., and Rutherford, M. J. (1997). Preeruption conditions and timing of dacite-andesite magma mixing in the 2.2 ka eruption at Mount Rainier. Journal of Geophysical Research: Solid Earth (1978–2012), 102(B9), 20069-20086.

Voight, B., Linde, A.T., Sacks, I.S., Mattioli, G.S., Sparks, R.S.J., Elsworth, D., Hidayat, D., Malin, P.E., Shalev, E., Widiwijayanti, C. and Young, S.R., (2006) Unprecedented pressure increase in deep magma reservoir triggered by lava-dome collapse. Geophysical Research Letters, 33(3).

Vona, A., Romano, C., Dingwell, D. B., and Giordano, D. (2011). The rheology of crystal-bearing basaltic magmas from Stromboli and Etna. Geochimica et Cosmochimica Acta, 75(11), 3214-3236.

Wadsworth, F.B., Vasseur, J., Scheu, B., Kendrick, J.E., Lavallée, Y. and Dingwell, D.B., (2016) Universal scaling of fluid permeability during volcanic welding and sediment diagenesis. Geology, 44(3), pp.219-222.

Wadsworth, F. B., Kennedy, B. M., Branney, M. J., von Aulock, F. W., Lavallée, Y., and Menendez, A. (2015). Exhumed conduit records magma ascent and drain-back during a Strombolian eruption at Tongariro volcano, New Zealand. Bull. Volcanol., 77(9), 1-10.

Wadsworth, F. B., Vasseur, J., Aulock, F. W., Hess, K. U., Scheu, B., Lavallée, Y., and Dingwell, D. B. (2014). Nonisothermal viscous sintering of volcanic ash. Journal of Geophysical Research: Solid Earth, 119(12), 8792-8804.

Webb, S. L., and Dingwell, D. B. (1990). Non-Newtonian rheology of igneous melts at high stresses and strain rates: Experimental results for rhyolite, andesite, basalt, and nephelinite. Journal of Geophysical Research: Solid Earth (1978–2012), 95(B10), 15695-15701.

Woods, A. W., and Koyaguchi, T. (1994). Transitions between explosive and effusive eruptions of silicic magmas. Nature, 370(6491), 641-644.

Woods, A. W. (1995). A model of vulcanian explosions. Nuclear engineering and design, 155(1), 345-357.

Wright, H. M. N., Roberts, J. J., and Cashman, K. V. (2006) Permeability of anisotropic tube pumice: model calculations and measurements, Geophys. Res. Lett., 33,TS16 2006.

Wright, H. M., and Weinberg, R. F. (2009). Strain localization in vesicular magma: Implications for rheology and fragmentation. Geology, 37(11), 1023-1026.

Zhu, W., Baud, P., Vinciguerra, S., and Wong, T. F. (2011). Micromechanics of brittle faulting and cataclastic flow in Alban Hills tuff. Journal of Geophysical Research: Solid Earth (1978–2012), 116(B6).

Figures:

Figure 1: Location of Volcàn de Colima in Mexico. (a) Google Earth™ satellite image of Volcán de Colima, showing each of the sample sites Volcancito, Montegrande, and La Lumbre (approximately 0.8, 3.5, and 6.7 km from the active vent, respectively). Inset shows the geographic location of Volcán de Colima within the Trans-Mexican Volcanic Belt (TMVB). (b) An aerial view of the main summit of Volcán de Colima, also showing the parasitic vent Volcancito, and the older, extinct member of the volcanic complex, Nevado de Colima.

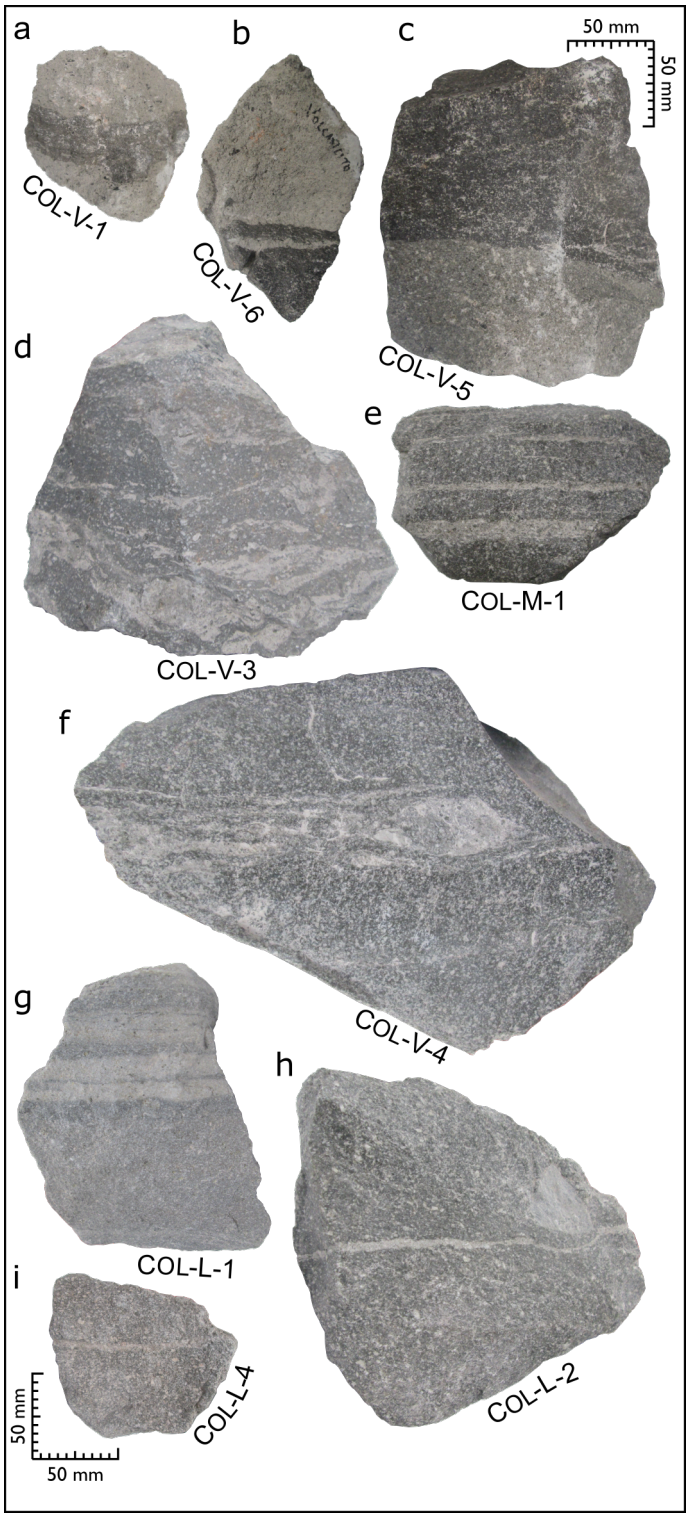

Figure 2: Collected discontinuity-bearing andesite blocks are shown in panels (a) to (i). Scale is the same for all blocks, and images are aligned so that the discontinuity is oriented more-or-less horizontally in each case. V, M, and L in each sample name refer to the sampling sites of Volcancito, Montegrande, and La Lumbre, respectively. We refer the reader to Table 1 for a detailed description of each block.

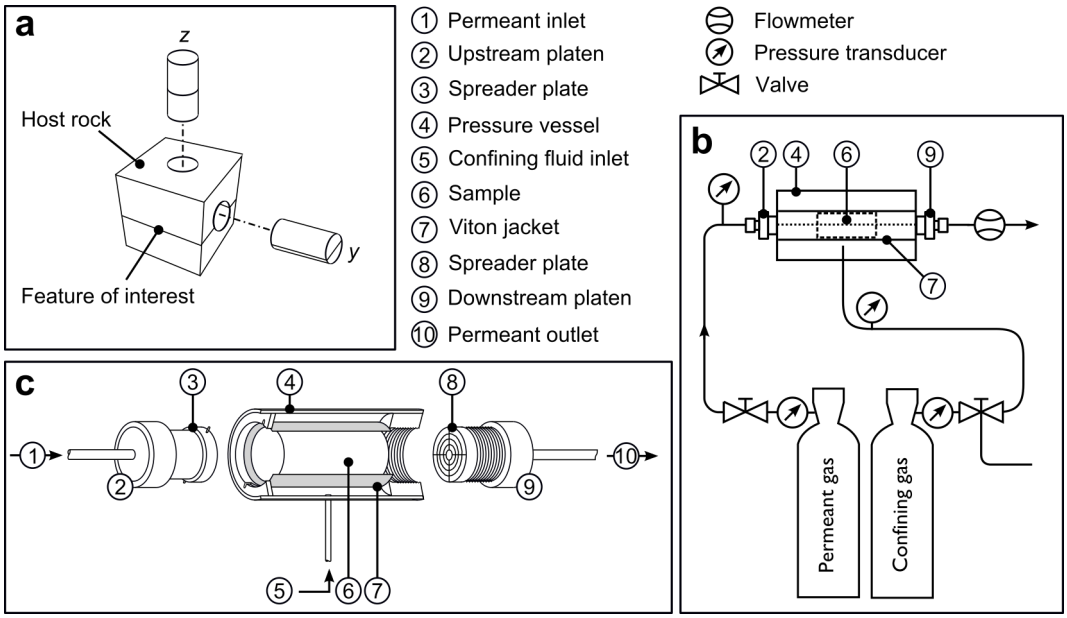

Figure 3: Anisotropic permeability measurements on banded rocks. (a) Orthogonal cores are obtained from each block with respect to the plane of the feature of interest. (b) Schematic of the benchtop steady-state permeameter used in this study. Both the permeant (pore fluid) and confining pressure gases are nitrogen. The sample is inserted into the annular viton jacket, which is secured within the pressure vessel shown in (c). The up- and downstream platens are screwed into position until both spreader plates are in firm contact with the sample. A confining pressure can then be applied to the sample by filling the annulus (the void space between the vessel and jacket) with gas. With this setup, the pressure differential ∇P between the upstream pressure transducer and atmospheric pressure downstream of the sample can be monitored at different volumetric flow rates, measured using the downstream flowmeter, during which time the system vents to the air. The confining pressure imposed on the sample and jacket (in these tests, 1 MPa) ensures that the through-flowing pore fluid does not leak around the sides of the sample. To ensure microstructural equilibration, the sample was left at this confining pressure of for a minimum of one hour prior to each test. Similarly, each measurement was only made once the gas flow through the sample had achieved steady-state equilibrium over time. Schematics not to scale.

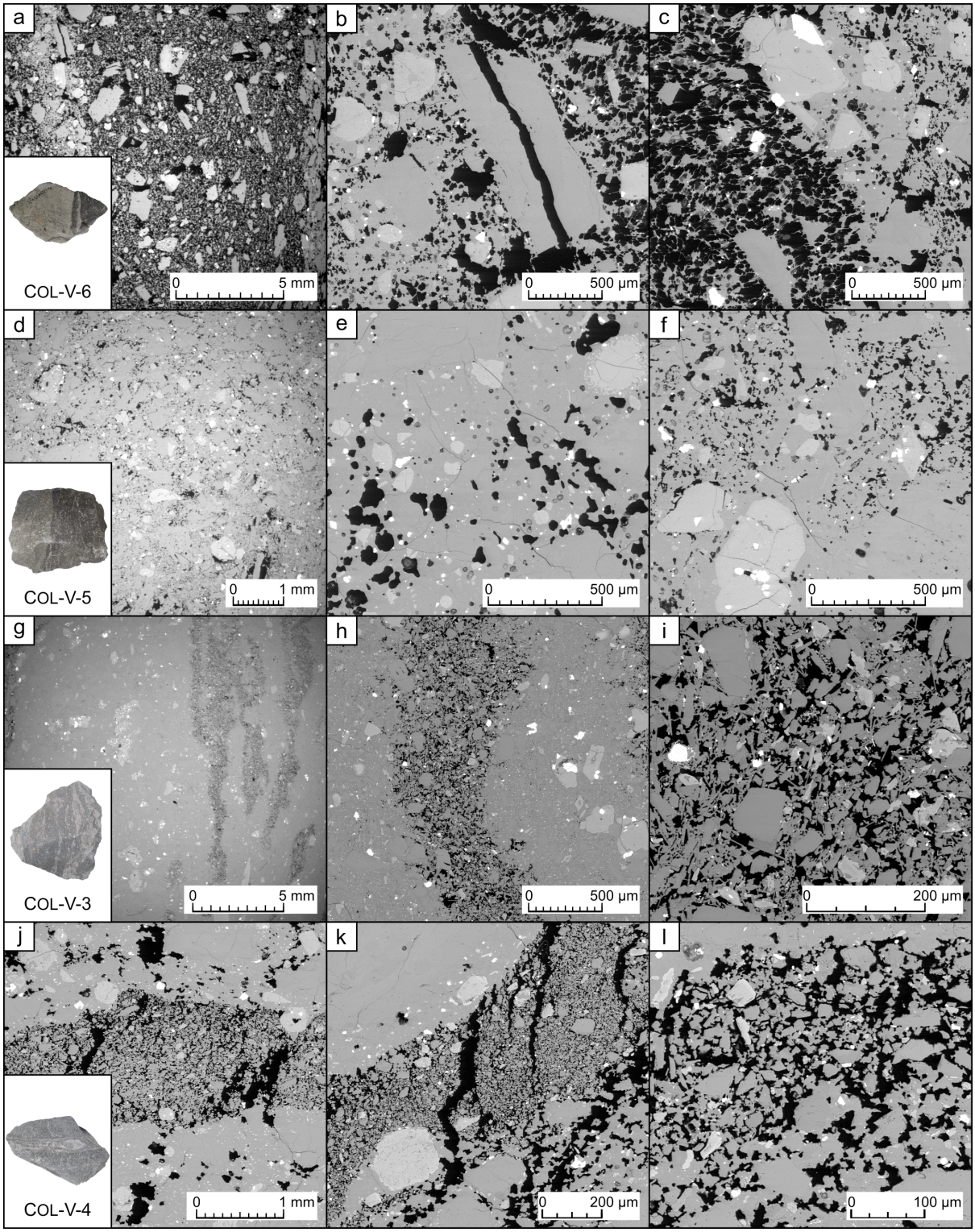
a
COL-V-6
0 5 mm
b
0 500 µm
c
0 500 µm
d
COL-V-5
0 1 mm
e
0 500 µm
f
0 500 µm
g
COL-V-3
0 5 mm
h
0 500 µm
i
0 200 µm
j
COL-V-4
0 1 mm
k
0 200 µm
l
0 100 µm

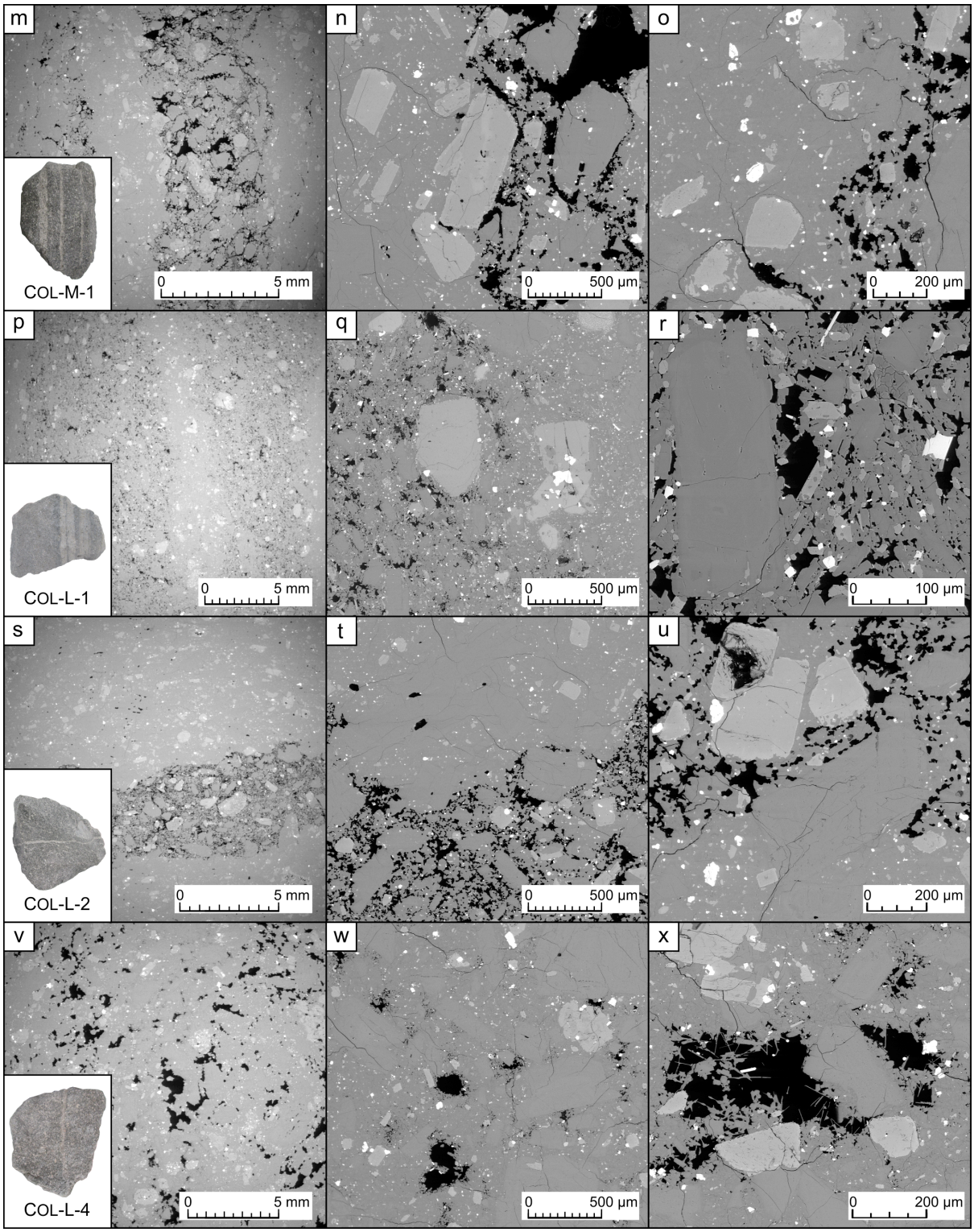

Figure 4: Examples of microstructure for eight samples. Each sample is shown inset, with three panels showing microstructure at varying scales. Porosity is shown as black in these and all subsequent SEM images. Note that the left-most panel of each row is an image of the whole thin section, cropped in order to avoid the visual distortion (*i.e.* the "fisheye" effect) resulting from the low magnification. (a) Sample COL-V-6, showing recurring bands of less-porous material within a highly

porous sample. (b) Large phenocryst in COL-V-6 which has been extensionally fractured and pulled in two by approximately 100 μm. (c) The transition from high porosity (left-hand-side) to low porosity (right-hand-side) regions of COL-V-6. Much of the porosity in the left-hand-side appears elongated perpendicular to the band (*i.e*. elongated horizontally in the image), whereas evidence of band-parallel directionality (vertical elongation in the image) can be seen in the lower-porosity region (right-hand-side). Refer to text for more discussion. (d) SEM image of sample COL-V-5. Note that the transition between pale and dense regions appears discrete at hand-sample scale (inset), but is less apparent in the microstructure. (e) Typical porosity within the paler part of the block (COL-V-5). It is notably more spherical or amœboid, as well as typically larger, than the porosity shown in (f), which comprises the darker region of the same block. (g) The variably anastomosed lenses of higher porosity of COL-V-3. A closer image (h) shows that the transition from dense to porous material occurs over a distance on the order of 100 μm. Inside the bands of COL-V-3 (i) we observe incipient ("point-to-point") welding, and possible evidence of needle-like vapour-phase crystallisation textures. (j) Sample COL-V-4, wherein discrete bands of increased porosity can be easily discerned. Closer images show extensional *en échelon* porosity (k) and variably-sized granular material (l). From the edge of the band towards its centre, an evolution from nonwelded fragments towards a partially welded medium can be seen (k, l). (m) Sample COL-M-1, wherein two of the three porous bands can be seen (oriented vertically). A closer image of the discontinuity is shown in (n), where it can be seen that phenocrysts intrude into the band. In (o), "feathery" groundmass textures can be seen, indicative of devitrification within COL-M-1. Panel (p) similarly shows the alternating bands of dense and relatively porous material in COL-L-1. The transition between these regions is diffuse, occurring over approximately 500 μm, shown in (q). As with sample COL-M-1, panel (r) shows that the largest pores in COL-L-1 are associated with phenocrysts. The band in sample COL-L-2 is shown in (s). The boundary between the host rock and the fracture is shown in greater detail in (t) and (u). Notably, the groundmass is entirely interconnected in (u), indicating that sintering of transiently granular material is well advanced. In the final sample, COL-L-4, the feature is manifest in a low-porosity band aligned vertically in (v) and the hand-sample image, inset. The band is notably diffuse, encompassing the relatively dense patch running more or less vertically through the centre of the image. In (w), the progression from relatively

spherical or amœboid pores to almost entirely infilled porosity can be discerned in more detail as one moves from the bottom to the top of the image. Within many of the pores of COL-L-4, variably-sintered material and vapour-phase crystallisation textures can be observed, as shown in (x).

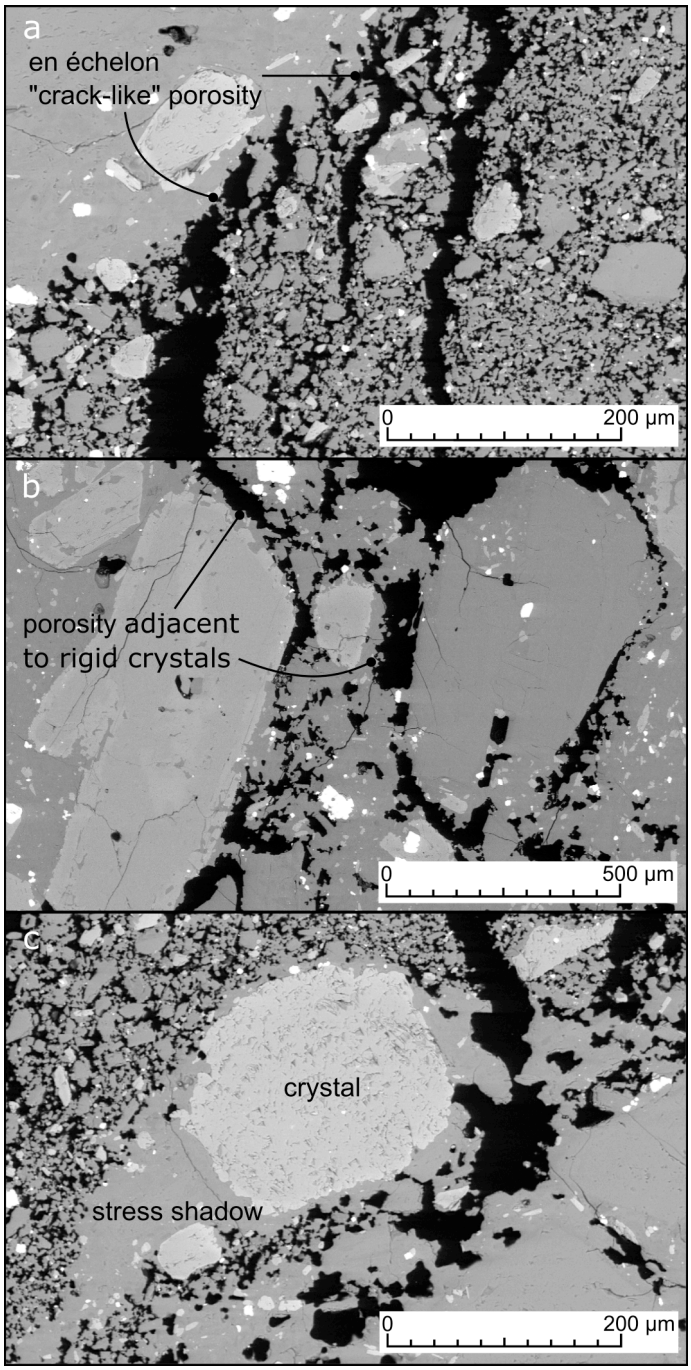

Figure 5: Evidence of shear-induced transtension (cavitation) in banded samples. (a) High aspect ratio *en échelon* porosity, indicative of extensional shearing in COL-V-4. In (b) and (c), porosity can be seen preferentially formed around the edge of large phenocrysts (in samples COL-M-1 and COL-V-4, respectively). (c) Local differences in stress are evidence by a tail of non-fragmental material, reflecting a stress shadow adjacent to a phenocryst.

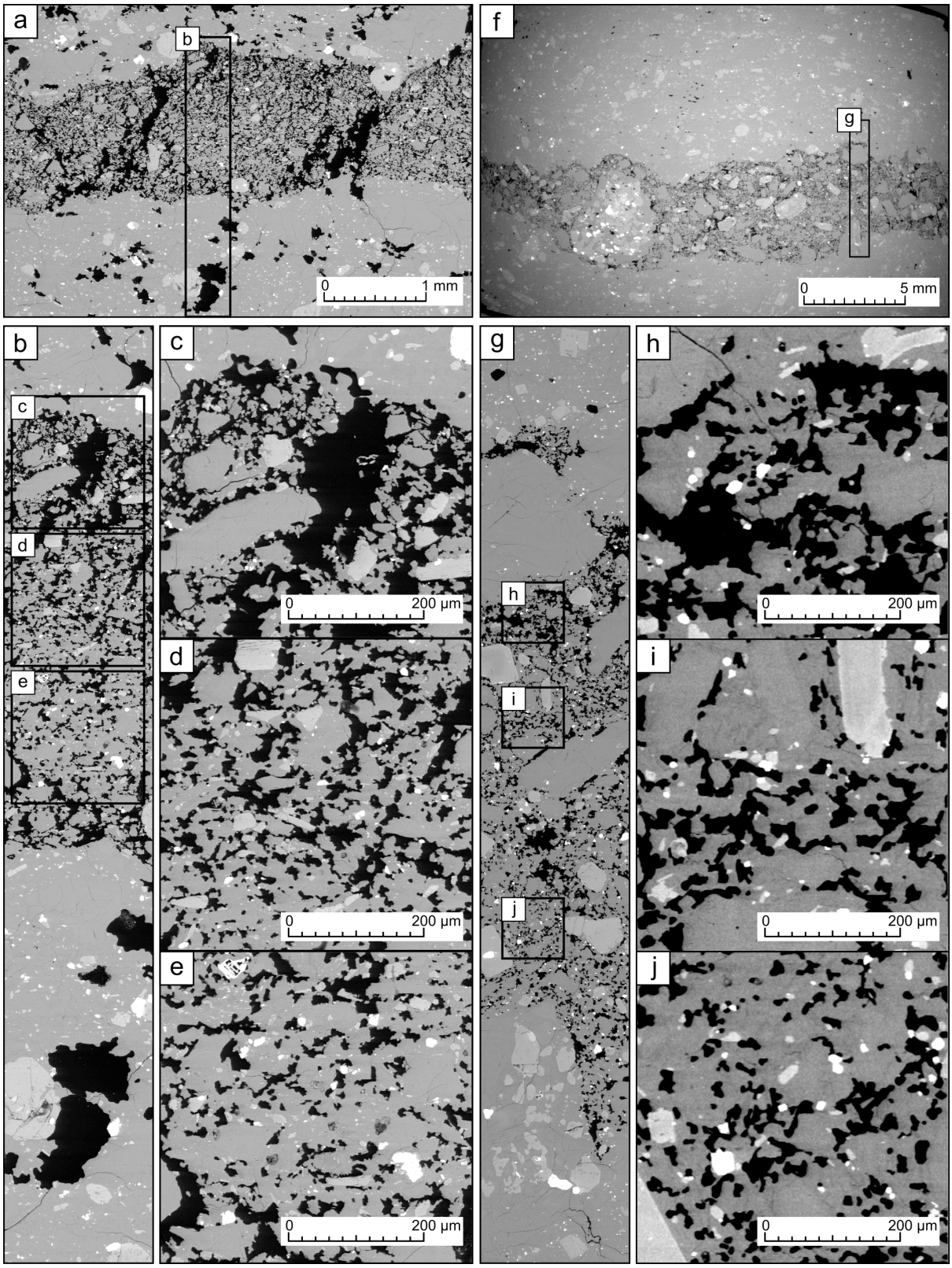

Figure 6: The evolution of sintering of granular fracture material. (a) Planar fracture in sample COL-V-4. (b) Detailed SEM images (c - e) are acquired from the edge and near the centre of the band. (c) At the edge of the fracture, discrete ash-sized fragments can be discerned, most of which retain their

angular form. For example, a cluster of discrete grains can be seen in the top-left of the panel. (d) Some rounding of fragments can be seen, and there is an increased connectivity of the groundmass. Both are indicative of incipient sintering. Characteristic "necks" can be observed forming between some of the formerly angular fragments; i.e. where there is a concave curvature of connecting groundmass between particle bodies, in contrast to the convex curvature of the particle surfaces. (e) Closer to the centre of the band, the groundmass is better connected, and porosity is increasingly more isolated relative to (c) and (d). This is evident throughout the panel, where numerous pores < 20μm in diameter can be discerned with little or no connectivity with their neighbouring pores. (f) Planar fracture in sample COL-L-2. (g) The location of detailed images (h - j) is shown, the first at the edge of the band, the latter two towards the centre. (h) As in (c), some discrete granular material can be observed within the void space, particularly in the bottom-right of the image. However, rounding of the fragments is more pronounced, suggesting more advanced sintering than their counterparts shown in (c). (i) Towards the middle of the fracture, the microstructure has transitioned from variably granular material within void space to a competent groundmass with variably connected porosity. Note that the pore shape is generally amœboid to spherical. Necking textures are pronounced in the centre-right and bottom-left of the image. (j) Similar textures to (i) are evident, but the image indicates notably poorer connectivity of the pores, suggestive of more advance sintering. Note that the characteristic shapes of the original granular material cannot be discerned.

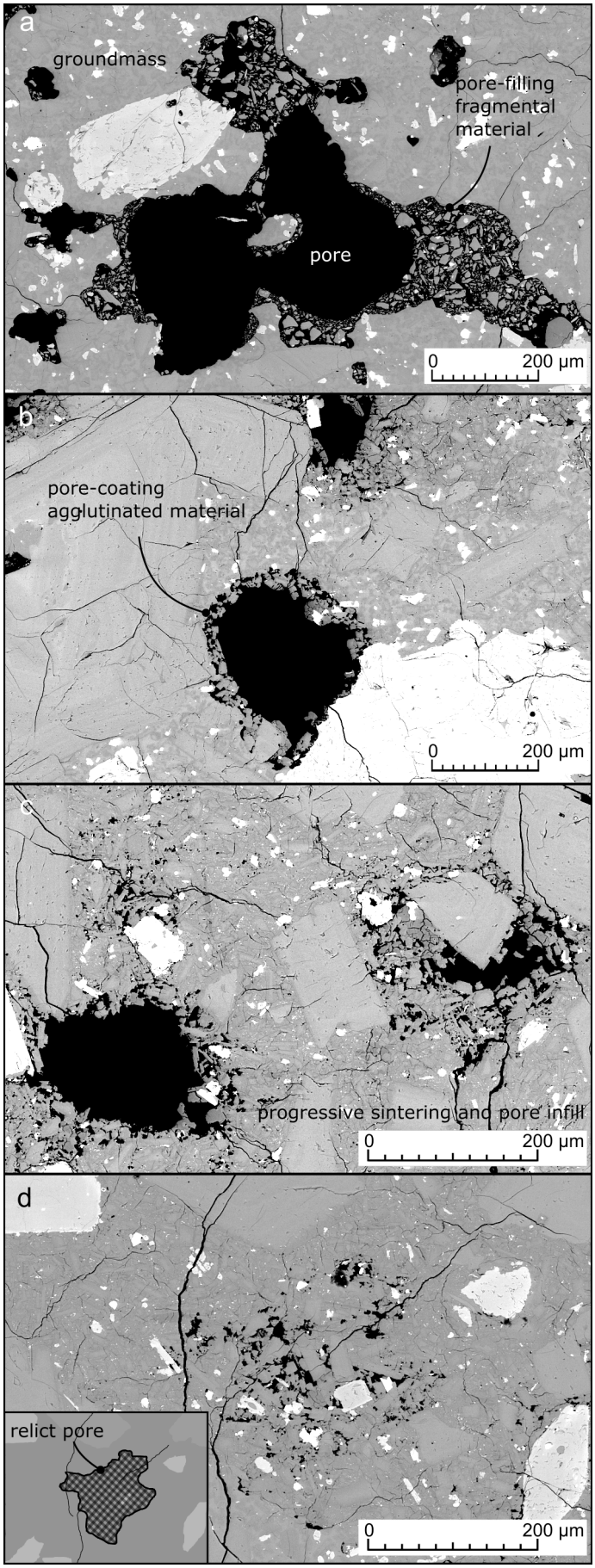
a
groundmass
pore-filling
fragmental
material
pore
0
200 µm
b
pore-coating
agglutinated material
0
200 µm
c
progressive sintering and pore infill
0
200 µm
d
relict pore
0
200 µm

Figure 7: Progressive pore infill in sample COL-L-4, from near the margin (a) towards the centre (d) of the band. (a) A pore, partially infilled with fragmental material. (b) Agglutinated material adhering to the pore wall. Textures shown in (c) indicate that the infilling material has progressively clogged up pores in this sample. Finally, in (d) the pore is almost entirely filled in, and the infilling material is well sintered. The previous extent of the pore is preserved as a patch of microporosity (sketched in inset).

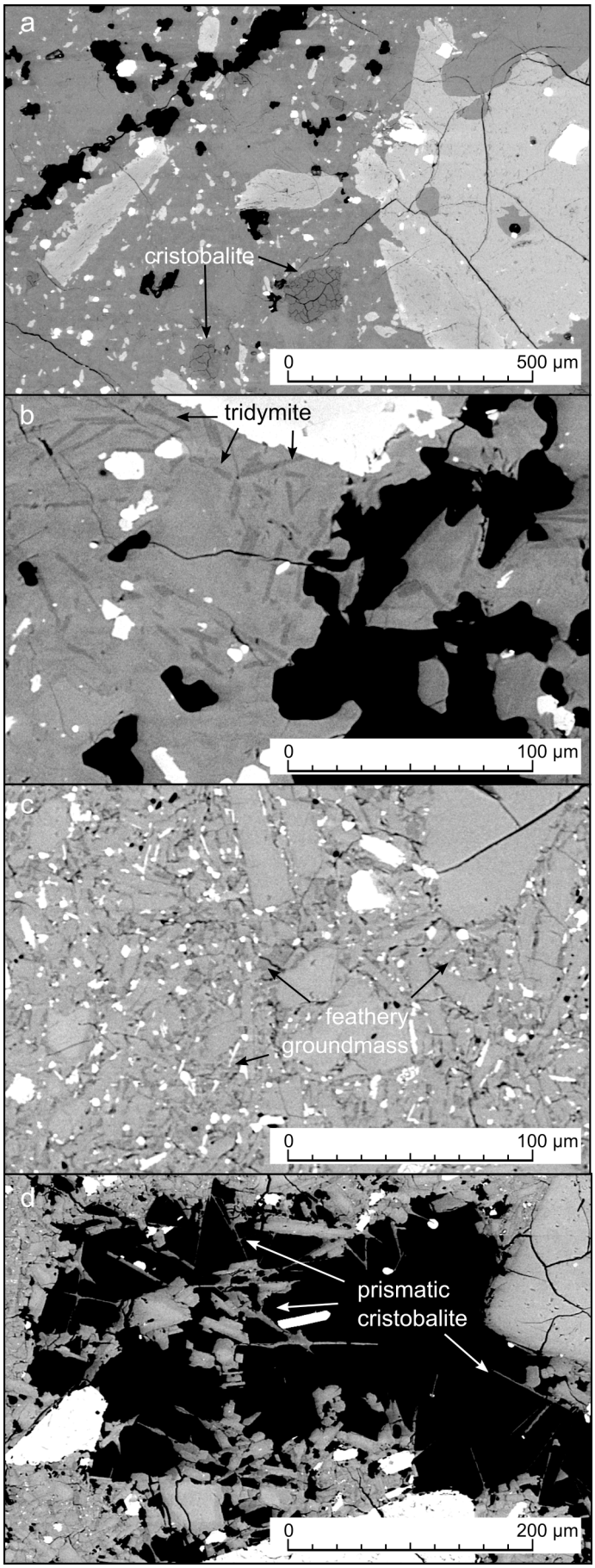
a
cristobalite
0
500 µm
b
tridymite
0
100 µm
c
feathery
groundmass
0
100 µm
d
prismatic
cristobalite
0
200 µm

Figure 8: Textural evidence for silica polymorphs. (a) Dark grey patches are cristobalite crystals, showing characteristic "fish-scale" cracking in sample COL-M-1. (b) Dark grey, high aspect ratio crystals are acicular tridymite (sample COL-L-2). (c) The groundmass of sample COL-V-3 has a "feathery" texture, indicative of devitrification of the groundmass (see Horwell *et al*., 2012; 2013). (d) High aspect ratio crystals inferred to be prismatic cristobalite are often seen growing into pore spaces (sample COL-L-4).

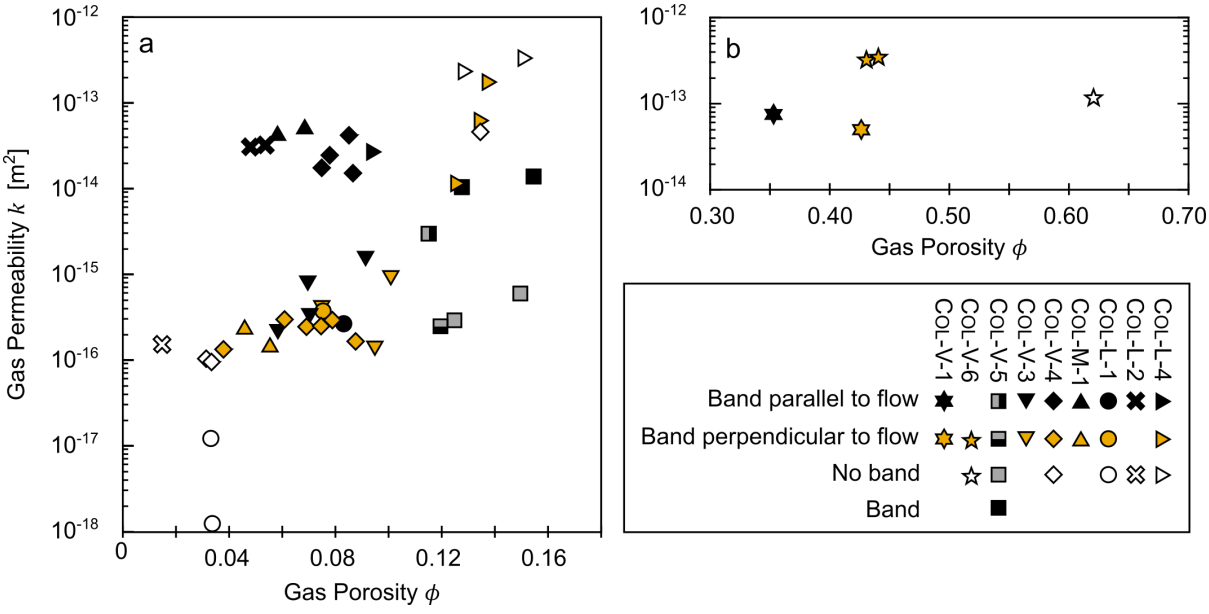

Figure 9: Connected gas porosity (ϕ) and gas permeability (k) data for all fifty core samples. (a) Low-porosity samples ($\phi < 20$). (b) High-porosity samples ($\phi > 30$). Note the difference in scale of the x-axis between either panel. Different blocks are indicated by different symbols, while the presence or orientation of a feature is given by the symbol colour. Measurement error is less than the symbol size in each case. Refer to text for discussion.

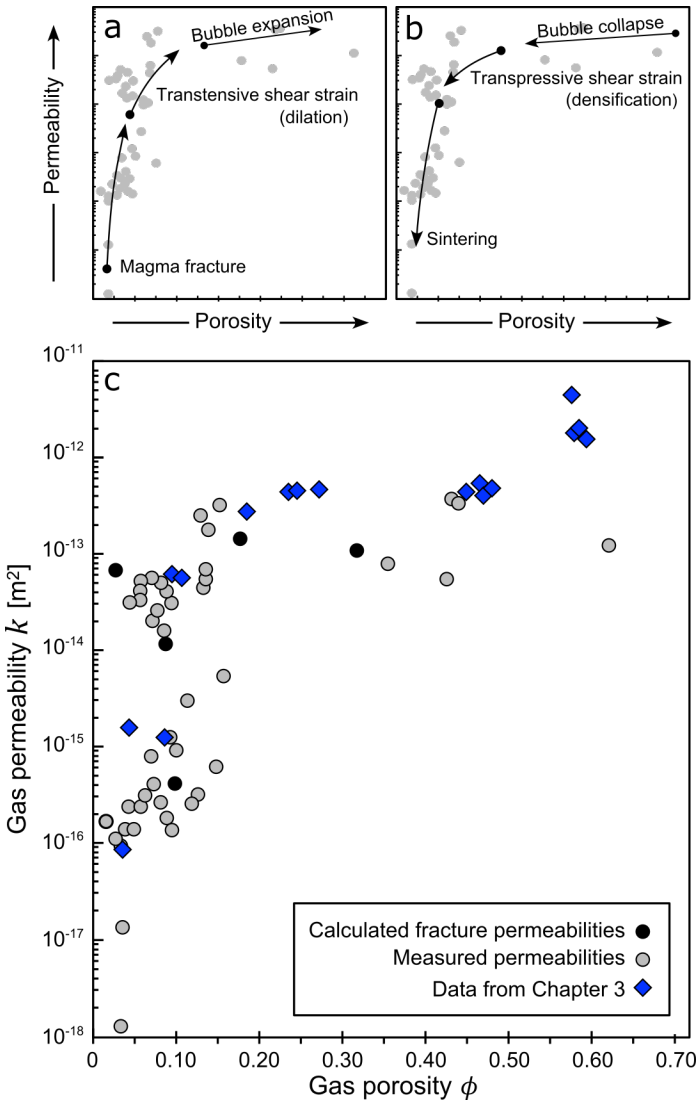

Figure 10: The influence of magmatic processes on the development of permeability, as predicted from our microstructural interpretations. (a) Dilatant (porosity-increasing) processes, including magma fracture, shear-induced extension, cavitation, and bubble expansion, exhibit a non-linear effect on permeability: at low porosities, large increases in permeability may be observed and vice versa. (b) Compactant or densifying processes—such as sintering, pore infill, and bubble collapse—similarly exert a large influence when the initial porosity is low, and only a slight influence when the initial porosity and permeability are high. (c) Collated permeability and porosity data. Despite the inclusion or orientation of the heterogeneities discussed throughout this study, the permeability-porosity data follow essentially the same trend as that of collected band-free samples (data taken from Farquharson *et al*., 2015). Further, the data for the bands themselves (calculated permeability from Equation 1 in

concert with 2D SEM-derived porosities: from Table 2, Table 4) also follow this trend. Measurement error is less than the symbol size in each case.

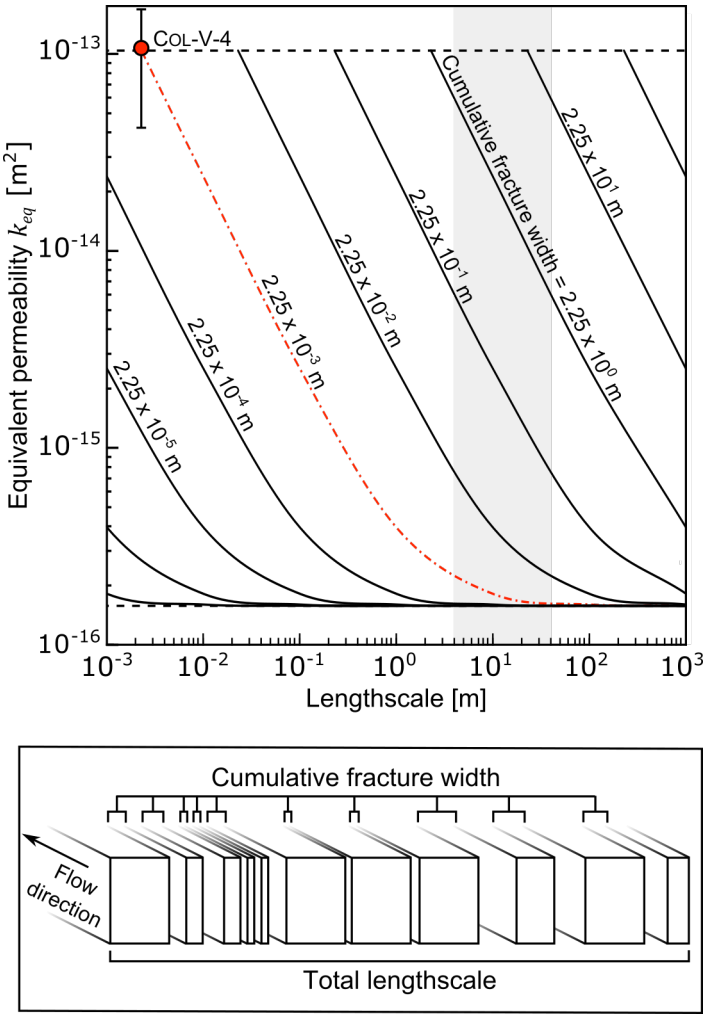

Figure 11: The scale-dependence of permeability anisotropy. Equivalent permeability (Equation 1) is shown for a fracture or set of fractures within porous magma. As the permeabilities of the fracture and the host material remain constant (defined by the upper and lower dashed lines respectively), equivalent permeability relies on both the considered lengthscale and the cumulative fracture width (*i.e.* number and width of fractures). Measured value of sample COL-V-4 is shown for reference. Note that $k_f \geq k_e \geq k_i$. The shaded area corresponds to the width of a volcanic conduit (see Noguchi *et al.*, 2008); red dashed line describes the influence of a 2.25 mm fracture with the fluid transport properties of that in sample COL-L-4. 1D upscaling model defines flow in parallel cracks, such that the total lengthscale is divided into parallel blocks or plates, shown inset. Refer to text for more discussion.

COL-V-1-Y 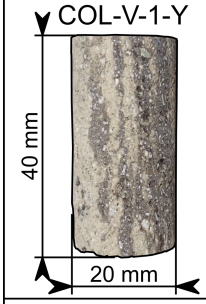	COL-V-1-Z 	COL-V-6-Z_1 	COL-V-6-Z_2 	COL-V-6-Z_3 
COL-M-1-Y_1 	COL-M-1-Y_2 	COL-M-1-Z_1 	COL-M-1-Z_2 	COL-L-1-Y_1 
COL-L-1-Y_2 	COL-L-1-Z_1 	COL-L-1-Z_2 	COL-V-5-Y_{BLACK} 	COL-V-5-Y_{BOTH} 
COL-V-5-Y_{GREY} 	COL-V-5-Z_{BLACK} 	COL-V-5-Z_{GREY} 	COL-V-5-Z_{BOTH} 	COL-L-4-Y_1 
COL-L-4-Y_2 	COL-L-4-Z_1 	COL-L-4-Z_2 	COL-L-4-Z_3 	COL-L-4-Z_4 

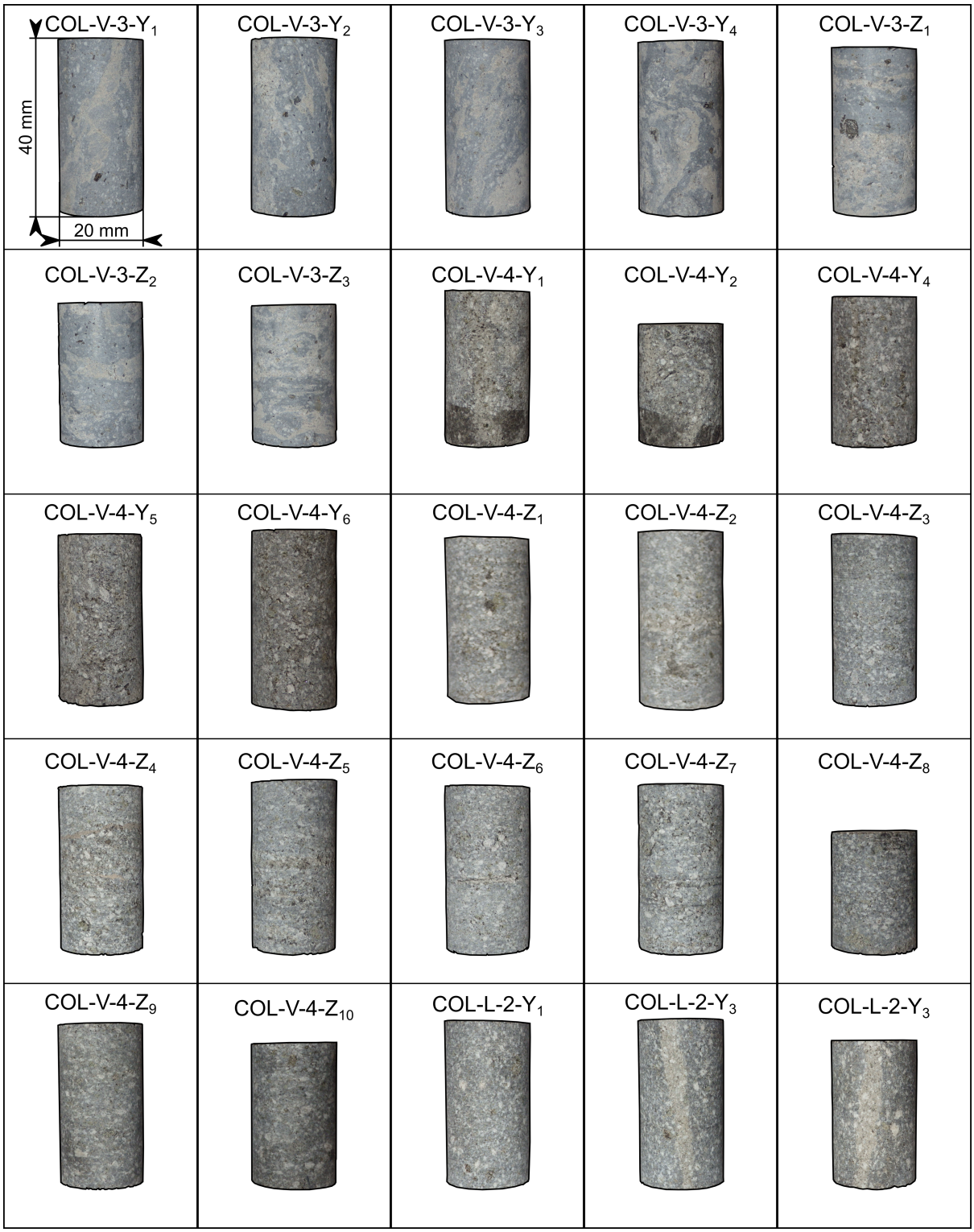

Figure A1: Photographs of the core samples measured in this study. Scale shown in the top left is the same for each panel. Sample names indicate sampling location (V, M, and L refer to Volcancito, Montegrande , La Lumbre, respectively: Figure 1a), and coring direction (Y and Z correspond to samples cored parallel and perpendicular to the feature of interest: Figure 3a).

Table 1: Block (hand-sample) descriptions, including reference to the corresponding photographs in Figure 2.

Block name	Photograph	Collection location	Block description
COL-V-1	Figure 2a	Volcancito	Pumiceous clast containing denser, darker grey portions, approximately 40 mm thick.
COL-V-6	Figure 2b	Volcancito	Pumiceous clast containing recurring denser, darker grey regions, from 10 to 40 mm thick.
COL-V-5	Figure 2c	Volcancito	Dense rock displaying two competent portions defined by their difference in colour (a light grey side and a dark grey side). Several small (cm - scale) xenoliths can be observed in the sample.
COL-V-3	Figure 2d	Volcancito	Dense, dark grey rock containing variously anastomosed lenses of lighter coloured material, ranging from around 5 to 40 mm in thickness.
COL-M-1	Figure 2e	Montegrande	Dark grey clast containing three light grey tabular bands ranging from 5 to 15 mm in thickness.
COL-V-4	Figure 2f	Volcancito	Large dense and glassy block, containing numerous anastomosing 1 - 10 mm thick bands of light grey, variably friable material. Some evidence of oxidation can be observed within the bands.
COL-L-1	Figure 2g	La Lumbre	Dense rock containing three tabular bands which are light grey in colour. Bands are approximately 5 mm in thickness.
COL-L-2	Figure 2h	La Lumbre	Dense glassy block containing a single through-cutting band, approximately 5 - 10 mm thick. The band appears to curve around a xenolith.
COL-L-4	Figure 2i	La Lumbre	Dark grey clast containing a tabular band 5 - 10 mm thick. The band is typically light grey, with brick-red oxidation visible.

Table 2: SEM-derived band and host-rock porosities, including the difference between the two ($\boldsymbol{\Delta\phi}$).

Sample	Band porosity	Host porosity	$\Delta\phi$
COL-V-6	0.23	0.50	-0.27
COL-V-5	0.09	0.09	0.00
COL-V-3	0.29	0.01	0.28
COL-V-4	0.32	0.06	0.26
COL-M-1	0.20	0.01	0.19
COL-L-1	0.10	0.03	0.07
COL-L-2	0.18	0.01	0.17
COL-L-4	0.03	0.13	-0.10

Table 3: Connected gas porosity and gas permeability data for core samples. Table also indicates whether the core was obtained parallel or perpendicular to the feature in the sample, and whether or not the feature was present in the core.

Sample	Gas porosity ϕ	Gas permeability	Core orientation with respect to flow direction	Feature

		k (m^2)		
COL-V-1-Y	0.35	7.98×10^{-14}	Parallel	Present
COL-V-1-Z	0.43	5.44×10^{-14}	Perpendicular	Present
COL-V-6-Z_1	0.43	3.42×10^{-13}	Perpendicular	Present
COL-V-6-Z_2	0.44	3.40×10^{-13}	Perpendicular	Present
COL-V-6-Z_3	0.62	1.18×10^{-13}	Perpendicular	Absent
COL-M-1-Y_1	0.07	5.16×10^{-14}	Parallel	Present
COL-M-1-Y_2	0.06	4.18×10^{-14}	Parallel	Present
COL-M-1-Z_1	0.06	1.46×10^{-16}	Perpendicular	Present
COL-M-1-Z_2	0.05	2.40×10^{-16}	Perpendicular	Present
COL-L-1-Y_1	0.08	2.84×10^{-16}	Parallel	Present
COL-L-1-Y_2	0.03	1.36×10^{-17}	Parallel	Absent
COL-L-1-Z_1	0.03	1.29×10^{-18}	Perpendicular	Absent
COL-L-1-Z_2	0.08	4.24×10^{-16}	Perpendicular	Present
COL-V-5-Y_{BLACK}	0.13	1.05×10^{-14}	Parallel	Present
COL-V-5-Y_{BOTH}	0.11	3.03×10^{-15}	Parallel	Present
COL-V-5-Y_{GREY}	0.15	6.24×10^{-16}	Parallel	Absent
COL-V-5-Z_{BLACK}	0.15	1.37×10^{-14}	Perpendicular	Present
COL-V-5-Z_{GREY}	0.13	2.90×10^{-16}	Perpendicular	Absent
COL-V-5-Z_{BOTH}	0.12	2.48×10^{-16}	Perpendicular	Present
COL-L-4-Y_1	0.13	2.40×10^{-13}	Parallel	Absent
COL-L-4-Y_2	0.09	3.18×10^{-14}	Parallel	Present
COL-L-4-Z_1	0.13	1.11×10^{-14}	Perpendicular	Present
COL-L-4-Z_2	0.15	3.30×10^{-13}	Perpendicular	Absent
COL-L-4-Z_3	0.14	6.21×10^{-14}	Perpendicular	Present
COL-L-4-Z_4	0.14	1.76×10^{-13}	Perpendicular	Present
COL-V-3-Y_1	0.07	3.45×10^{-16}	Parallel	Present
COL-V-3-Y_2	0.07	8.03×10^{-16}	Parallel	Present
COL-V-3-Y_3	0.06	1.56×10^{-16}	Parallel	Present
COL-V-3-Y_4	0.09	1.22×10^{-15}	Parallel	Present
COL-V-3-Z_1	0.10	1.41×10^{-16}	Perpendicular	Present
COL-V-3-Z_2	0.08	4.10×10^{-16}	Perpendicular	Present
COL-V-3-Z_3	0.10	8.98×10^{-16}	Perpendicular	Present
COL-V-4-Y_1	0.09	4.23×10^{-14}	Parallel	Present
COL-V-4-Y_2	0.09	1.56×10^{-14}	Parallel	Present
COL-V-4-Y_4	0.08	1.78×10^{-14}	Parallel	Present
COL-V-4-Y_5	0.13	4.70×10^{-14}	Parallel	Present

COL-V-4-Y_6	0.08	2.41×10^{-14}	Parallel	Present
COL-V-4-Z_1	0.06	3.00×10^{-16}	Perpendicular	Absent
COL-V-4-Z_2	0.08	2.99×10^{-16}	Perpendicular	Present
COL-V-4-Z_3	0.04	1.29×10^{-16}	Perpendicular	Absent
COL-V-4-Z_4	0.08	2.50×10^{-16}	Perpendicular	Present
COL-V-4-Z_5	0.09	1.70×10^{-16}	Perpendicular	Present
COL-V-4-Z_6	0.04	1.32×10^{-16}	Perpendicular	Present
COL-V-4-Z_7	0.07	2.53×10^{-16}	Perpendicular	Present
COL-V-4-Z_8	0.06	2.83×10^{-16}	Perpendicular	Present
COL-V-4-Z_9	0.03	9.77×10^{-17}	Perpendicular	Absent
COL-V-4-Z_{10}	0.03	1.05×10^{-16}	Perpendicular	Absent
COL-L-2-Y_1	0.01	1.77×10^{-16}	Parallel	Absent
COL-L-2-Y_2	0.05	3.09×10^{-14}	Parallel	Present
COL-L-2-Y_3	0.05	3.30×10^{-14}	Parallel	Present

Table 4: Mean permeabilities and dimensions used to calculate the permeability of the feature for five samples. Note that we use "fracture" permeability to refer to the permeability of any of the discussed features, regardless of genesis.

Sample	Intact permeability k_i (m^2)	Equivalent permeability k_e (m^2)	Sample area (mm^2)	Fracture area (mm^2)	Fracture permeability (m^2)	Relative permeability k_r
COL-V-5	1.37×10^{-16}	N/A[1]	N/A[a]	N/A[a]	1.21×10^{-14}	87.32
COL-V-4	1.58×10^{-16}	2.94×10^{-14}	312.84	74.1581	1.04×10^{-13} [2]	657.23
COL-L-1	1.36×10^{-17}	2.84×10^{-16}	312.87	128.23	3.90×10^{-16}	27.68
COL-L-2	1.77×10^{-16}	3.19×10^{-14}	310.92	58.52	1.37×10^{-13} [3]	773.01
COL-L-4	2.40×10^{-13}	3.18×10^{-14}	308.19	44.80	6.67×10^{-14}	-0.72

[1] for COL-V-5 (Figure 2c) it was possible to obtain cores containing only the host material or only the band (see Table 3). Thus we have a discrete measure of the band permeability relative to the initial material, and no calculation is necessary.

[2] Value shown is mean value determined from fracture permeabilities of two samples COL-V-4-Y_1, -Y_2. Values range from 1.67×10^{-13} - 4.12×10^{-14}.

[3] Value shown is mean value determined from fracture permeabilities of two samples COL-L-2-Y_1, -Y_2. Values range from 1.32×10^{-13} - 1.42×10^{-13}.